Unique aqueous Li-ion/sulfur chemistry with high energy density and reversibility

Chongyin Yang[a], Liumin Suo[a], Oleg Borodin[b], Fei Wang[a], Wei Sun[a], Tao Gao[a], Xiulin Fan[a], Singyuk Hou[a], Zhaohui Ma[a], Khalil Amine[c], Kang Xu[b,1], and Chunsheng Wang[a,1]

[a]Department of Chemical and Biomolecular Engineering, University of Maryland, College Park, MD 20740; [b]Electrochemistry Branch, Sensor and Electron Devices Directorate, Power and Energy Division, US Army Research Laboratory, Adelphi, MD 20783; and [c]Chemical Sciences and Engineering Division, Argonne National Laboratory, Argonne, IL 60439

Edited by Thomas E. Mallouk, The Pennsylvania State University, University Park, PA, and approved May 9, 2017 (received for review March 8, 2017)

Leveraging the most recent success in expanding the electrochemical stability window of aqueous electrolytes, in this work we create a unique Li-ion/sulfur chemistry of both high energy density and safety. We show that in the superconcentrated aqueous electrolyte, lithiation of sulfur experiences phase change from a high-order polysulfide to low-order polysulfides through solid–liquid two-phase reaction pathway, where the liquid polysulfide phase in the sulfide electrode is thermodynamically phase-separated from the superconcentrated aqueous electrolyte. The sulfur with solid–liquid two-phase exhibits a reversible capacity of 1,327 mAh/(g of S), along with fast reaction kinetics and negligible polysulfide dissolution. By coupling a sulfur anode with different Li-ion cathode materials, the aqueous Li-ion/sulfur full cell delivers record-high energy densities up to 200 Wh/(kg of total electrode mass) for >1,000 cycles at ∼100% coulombic efficiency. These performances already approach that of commercial lithium-ion batteries (LIBs) using a nonaqueous electrolyte, along with intrinsic safety not possessed by the latter. The excellent performance of this aqueous battery chemistry significantly promotes the practical possibility of aqueous LIBs in large-format applications.

water-in-salt | rechargeable aqueous battery | aqueous sulfur battery | gel polymer electrolyte | phase separation

In the past two decades, rechargeable lithium-ion batteries (LIBs) have revolutionized consumer electronics with their high energy density and excellent cycling stability, and are the state-of-the-art candidates for applications ranging from kilowatt hours for electric vehicles up to megawatt hours for grids (1, 2). The latter applications in large-format present much more stringent requirements for safety, cost, and environmental friendliness, besides energy density and cycle life. The shortcomings of LIB are mostly due to the flammable and toxic nonaqueous electrolytes and moderate energy densities (<400 $Wh{\cdot}kg^{-1}$) provided by the electrochemical couples currently used (3). Among the various "beyond Li-ion" high-energy chemistries (>500 $Wh{\cdot}kg^{-1}$) explored currently, the nonaqueous lithium/sulfur (Li/S) battery based on sulfur as a cathode (theoretical capacity of 1,675 $mAh{\cdot}g^{-1}$) and metallic lithium as an anode seems to be the most practical, as evidenced by the mushrooming literature and significant advances in this system in the past 5 y (4–7). However, commercialization of this system still faces challenges because of severe safety concerns associated with the dendrite growth of metallic Li anode in highly inflammable ether-based electrolytes (8), and the high self-discharge associated with parasitic shuttling of the intermediate polysulfide species. Moreover, the moisture-sensitive nature of the nonaqueous electrolyte would contribute significantly to the cost of the Li/S battery pack due to the stringent moisture-exclusion infrastructure required during the manufacturing, processing, and packaging of the cells. The indispensable accessories for safety and thermal management would further drive up the cost.

Replacement of the nonaqueous electrolyte by its aqueous counterpart is always tantalizing, because it would essentially eliminate safety, toxicity, and at least part of the cost concerns (9–11). In particular, wide electrochemical stability windows (>3.0 V) comparable to those of nonaqueous electrolytes have been recently demonstrated by water-in-salt (WiS) and water-in-bisalt (WiBS) electrolytes. With water molecules still far outnumbering that of Li salts, this class of completely nonflammable WiS and WiBS electrolytes realized a dramatic improvement in safety, while placing many Li-ion and even beyond Li-ion chemistries within the reach of aqueous electrolytes (12, 13). Historically, it has been very challenging to use elemental sulfur as the cathode material in aqueous electrolytes, primarily because of the high solubility of short-chain lithium polysulfide (Li_2S_x, $x < 6$) and Li_2S in aqueous media, and the strong parasitic shuttling reaction occurring thereafter (14). A compromise approach used aqueous solution of lithium polysulfide as the liquid active cathode (catholyte), but only 61% of the theoretical capacity was accessed in the Li_2S_4/Li_2S redox couple (15–17). The hydrogen evolution in this aqueous system and the side reaction between the Li_2S_4/Li_2S and H_2O have to be suppressed to achieve high coulombic efficiency. A Li metal anode can be used, but only after a dense Li-ion-conducting ceramic layer is engineered on the Li surface to prevent Li dendrite formation and prevent the reaction of Li anode from aqueous catholyte (17).

However, the reported electrochemical stability windows of the superconcentrated aqueous electrolytes (WiS, WiBS) were >3.0 V, with cathodic and anodic limits located in the vicinity of ∼1.9 V and ∼4.9 V vs. Li, respectively. This window would comfortably envelop the lithiation/delithiation reactions of high-capacity

Significance

Sulfur as an anode coupled with a lithium-ion intercalation cathode in the superconcentrated aqueous electrolyte creates a unique Li-ion/sulfur chemistry, realizing the highest energy density ever achieved in aqueous batteries, along with high safety and excellent cycle-life. Mechanism investigation finds that the reversible sulfur lithiation/delithiation in such an aqueous electrolyte proceeds with fast kinetics that significantly differ from that in nonaqueous systems, whereas polysulfides' insolubility in such an aqueous electrolyte essentially eliminates the parasitic shuttling. The excellent performances of Li-ion/sulfur cells not only find an application of "water-in-salt" electrolyte for beyond Li-ion chemistries, more importantly, an alternative pathway is provided to solve the "polysulfide shuttling" that has been plaguing the sulfur chemistries in nonaqueous electrolytes.

Author contributions: C.Y., L.S., O.B., F.W., K.A., K.X., and C.W. designed research; C.Y., L.S., O.B., F.W., W.S., T.G., X.F., S.H., and Z.M. performed research; C.Y., O.B., F.W., W.S., T.G., X.F., S.H., Z.M., K.A., K.X., and C.W. analyzed data; and C.Y., L.S., O.B., F.W., S.H., K.A., K.X., and C.W. wrote the paper.

The authors declare no conflict of interest.

This article is a PNAS Direct Submission.

[1]To whom correspondence may be addressed. Email: cswang@umd.edu or conrad.k.xu.civ@mail.mil.

This article contains supporting information online at www.pnas.org/lookup/suppl/doi:10.1073/pnas.1703937114/-/DCSupplemental.

sulfur materials at the anode side and transition metal oxide materials at the cathode side. The electrochemical coupling of a sulfur anode and an intercalation cathode would thus create a new cell chemistry without Li metal, which is based on Li^+ intercalation/deintercalation at the cathode, and conversion reaction of sulfur species at anode. This Li-ion/sulfur chemistry (Li^+/S) can deliver theoretic energy densities up to 260 Wh·kg^{-1}, and combines the high capacities of a cheap sulfur anode and mature LIB cathode, as well as the intrinsic safety of an aqueous electrolyte. Additional benefits include substantial cost reduction at the battery module or pack level, via elimination of moisture-free infrastructures for processing and fabrication, and the possible simplification of the safety management.

In this work, we demonstrate this highly reversible aqueous Li^+/S chemistry using a simple sulfur/carbon composite as the anode and LiMO ($LiMn_2O_4$ and $LiCoO_2$) as the cathodes. Through in situ and ex situ spectroscopic means during electrochemical reactions, the unique lithiation/delithiation mechanism of sulfur in WiBS electrolyte was revealed to proceed reversibly in a solid–liquid phase. A total of 80% (1,327 mAh·g^{-1}) of sulfur theoretical capacity (1,675 mAh·g^{-1}) was accessed with excellent reversibility, as evidenced by capacity retention of 86% for 1,000 cycles. This outstanding performance is attributed to the phase separation of S/polysulfide solid–liquid phase from high-concentration aqueous electrolytes, where the liquid WiBS electrolyte functions in a similar manner as solid electrolyte in isolating the polysulfide species generated at anode from LiMO cathodes, thus eliminating the parasitic shuttlings that have been plaguing the nonaqueous Li/sulfur chemistry. When the sulfur anode was paired with typical LIB cathode materials like $LiMn_2O_4$ or high-voltage $LiCoO_2$, energy densities of 135~200 Wh·kg^{-1} were delivered at full cell level. These findings suggest that safety, cost, environmental considerations, and energy density requirements could be simultaneously achieved by the aqueous Li^+/S battery for large-scale applications, such as smart-grid storage or automotive power systems.

Results

Electrochemical Behaviors of Sulfur in WiBS Aqueous Electrolyte. The electrochemical behaviors of a sulfur–Ketjen black (S-KB) carbon composite electrode in WiBS electrolyte and in typical organic electrolyte were investigated with cyclic voltammetry. WiBS electrolyte was obtained by dissolving two Li salts, lithium bis(trifluoromethane sulfonyl)imide (LiTFSI) and lithium trifluoromethane sulfonate (LiOTf) at 21 and 7 mol·kg^{-1}, respectively, in water at 25 °C. Using two lithium salts allows us to circumvent the solubility limits of each single lithium salt in water, hence reaching the highest salt concentration possible (13, 18). The extremely high concentration therein provides an expanded stability window thanks to the formation of a dense and protective solid electrolyte interphase (SEI) and the reduced water activity (13); it is also a key to manage stable phase-separation of liquid reaction intermediate and liquid electrolyte, which will be fully discussed below. Reversible lithiation/delithiation reaction of sulfur in this 28-mol·kg^{-1} electrolyte was observed at 2.46 and 2.65 V, respectively (Fig. 1*A*). Although the potential for hydrogen evolution at pH ~7.0 is known to be ~2.63 V vs. Li, the SEI suppresses the reduction of water molecules down to the potential of ~1.9 V, hence making the reversible lithiation/delithiation reaction possible. Upon closer comparison with the well-known redox processes of sulfur in nonaqueous media at 2.1~2.4 V (Fig. 1*A*, black dashed line) (19), an apparent positive shift of ~0.3 V occurred in the aqueous solution, which has been observed previously and attributed to the high Li salt concentration in WiBS electrolyte (12). More noticeable is the drastic change from the characteristic two-stage lithiation process in nonaqueous media to a seemingly single-stage redox process in aqueous media, as well as the much reduced potential hysteresis in the latter. Such changes are more visually obvious in the corresponding voltage profiles obtained in galvanostatic mode (Fig. 1*B*), where a single, well-defined plateau at ~2.5 V represents the discharge/charge of S-KB in the WiBS electrolyte, significantly differing from the two plateaus found at ~2.3 and 2.1 V in nonaqueous electrolyte (20). Apparently, the electrochemical reaction of sulfur in this superconcentrated aqueous electrolyte proceeds via a new reaction mechanism that is hitherto unknown. What we see in Fig. 1 should be a previously unobserved aqueous sulfur chemistry.

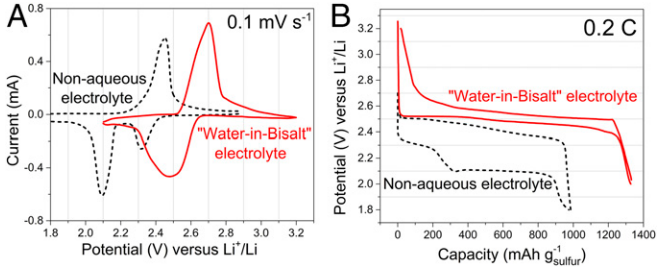

Fig. 1. Electrochemical performance of sulfur in aqueous electrolyte. (*A*) Cyclic voltammograms of S-KB composite at 0.1 mV·s^{-1} in aqueous electrolyte (red solid line) and nonaqueous electrolyte (black dashed line). (*B*) Typical voltage profiles of S-KB composite at constant current (0.2C) in aqueous electrolyte (red solid line) and nonaqueous electrolyte (black dashed line).

The typical two-plateau discharge curve obtained in nonaqueous media has been attributed to the solid-to-liquid (sulfur to dissolved high-order polysulfide) reaction, and liquid-to-solid (high-order polysulfides to low-order sulphide solid) reaction (21–23). The single-stage discharge plateau in WiBS electrolyte, however, suggested that the redox processes of sulfur undergo a single solid–liquid reaction, which proceeds with ultrafast kinetics; this is also consistent with the finding of Li_2S product formed during early charging, as discussed hereafter. As a result, a reversible capacity of 1,338 mAh·g^{-1} was achieved based on the sulfur mass at a current density of 335 mA·g^{-1} (0.2C), which is 80% of the theoretical capacity and comparable with the best results achieved in nonaqueous electrolyte (4).

Reaction Mechanism of Sulfur Anode in WiBS Electrolyte. To fully understand this sulfur chemistry in WiBS electrolyte, we used in situ Raman spectroscopy to monitor the transformation of polysulfide species in the S-KB anode at different states of charge (SOC) during the third charge of an S-KB/$LiMn_2O_4$ full cell (Fig. 2*A*). The fully discharged (delithiated) S-KB anode (SOC = 0%, corresponding to the fully charged state of sulfur when used as cathode in nonaqueous electrolyte) showed conspicuous peaks (indicated by yellow region in Fig. 2*A*) corresponding to elemental sulfur (α-S_8) at 81, 151, 217, and 470 cm^{-1} (24). Based on the normalized intensity ratio, the estimated amount of α-S_8 exponentially declines to nearly zero before the SOC reaches 25%, suggesting a surprisingly rapid and full consumption of S_8 by lithiation (Fig. 2*C*). A sharp peak at 339 cm^{-1}, which was assigned to the long-chain polysulfide species S_6^{2-} (25, 26), appeared at SOC = 25% but disappeared after SOC = 75%. Meanwhile, a small peak at 234 cm^{-1}, which was attributed to the bending mode of S_4^{2-}, gradually grew after SOC = 25% during charge (27). At the final stage of charge (SOC = 100%), a Li_2S peak located at 371 cm^{-1} appeared. These results clearly show the very rapid procession from elemental sulfur to long-chain polysulfides and then to the fully lithiated form Li_2S (i.e., S_8 → long chain Li_2S_x → short chain Li_2S_x → Li_2S). The fast kinetic drastically differs from the reduction of sulfur in nonaqueous media. In the aqueous media, an obvious lift-up occurs in the range of 65–300 cm^{-1} (Fig. 2*A*) with a peak at 80 cm^{-1} for SOC ≥ 50%. To investigate these peaks further, the Raman spectra of

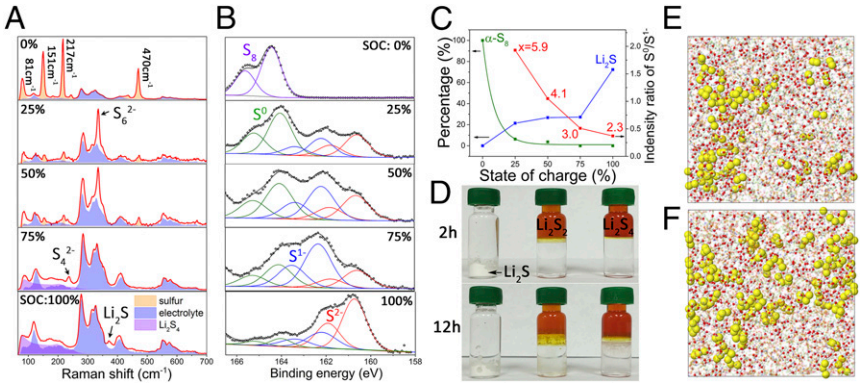

Fig. 2. In situ and ex situ studies of redox intermediate for sulfur anode. (*A*) In situ Raman spectra of the S-KB anode in full cell after being charged to specific SOC. Red lines are experimental data, and colored areas correspond to deconvoluted individual components. (*B*) XPS S 2*p* spectra of S-KB anode in full cell after being charged to specific states. Black dotted lines are experimental data, black lines are overall fitted data, and colored solid lines are fitted individual chemical states: $2p_{3/2\text{-purple}}(S_8)$ 164.4 eV; $2p_{3/2\text{-green}}(S^0)$ 164.0 eV; $2p_{3/2\text{-blue}}(S^{1-})$ 162.2 eV; and $2p_{3/2\text{-red}}(S^{2-})$ 160.7 eV. (*C*) The estimated content ratios of element S_8 (green), Li_2S (blue), and LiPS at specific SOCs. (*D*) Visual observation of the insolubilities for Li_2S and short-chain LiPS (Li_2S_2 and Li_2S_4) in WiBS electrolyte. A Li_2S white powder remains insoluble in clear aqueous electrolyte for 12 h. Jacinth solution on the top of bottle is Li_2S_2 or Li_2S_4 dissolved in water phase, which is separated from the clear aqueous electrolyte (salt phase) on the bottom. (*E* and *F*) Projections of MD simulation boxes highlighting Li_2S_4 (*F*) and Li_2S_2 (*E*) polysulfide anions (yellow) and water (O, red; H, white) separating in WiBS electrolyte at 333 K, respectively.

element sulfur powder, pure Li_2S powder, Li_2S_4 in aqueous solution, and WiBS electrolyte were analyzed (*SI Appendix*, Fig. S1). The peaks in the range of 65–300 cm^{-1} with a peak at 80 cm^{-1} for the S-KB anode were well fitted to the Raman spectra of water-solvated polysulfide mixture (Li_2S_4, purple area). Therefore, the Li_2S_4 manages to extract H_2O from WiBS electrolyte to form a Li_2S_4-anolyte, which is immiscible with the bulk WiBS electrolyte (Fig. 2*D*). Note that the dissolved lithium polysulfide (LiPS) only shows a wide peak at 80 cm^{-1}. Hence, sharp peaks for S_6^{2-} at SOC = 25% and for S_4^{2-} at SOC = 75% can only be attribute to solid phase of LiPS. A more direct observation of solid–liquid mixed polysulfide phase was confirmed by replacing an S-KB anode with sulfur coated on aluminum mesh (denoted as S@Al hereafter) that was horizontally placed on the top surface of WiBS electrolyte. The Raman spectra of the charged S@Al electrode showed individual traces of both liquid and solid polysulfide (*SI Appendix*, Fig. S2). This observation unambiguously reveals that the reaction intermediate (polysulfide) exist in both solid and liquid phase, where the liquefied polysulfides would have been confined by pore structure of carbon matrix and hence phase separated from WiBS in our full cells. Further confirmations of solid–liquid mixed phase of S-KB came from the electrochemistry performances of the washed S-KB at different SOC (*SI Appendix*, Fig. S3). After charging to states of 50%, 75%, and 100%, the S-KB electrodes were disassembled and washed using anhydrous dimethoxyethane (DME) for serval times to remove the liquid polysulfides, and then reassembled to measure the residual low-order solid polysulfides. After removing liquid phase and long-order LiPS intermediate, the remaining low-order solid polysulfides still can provide >70% of initial capacities. In diluted aqueous solutions, the long-chain species Li_2S_x ($x > 4$) are considered insoluble due to their relatively less-polar nature, whereas the short-chain species Li_2S_x ($x \leq 4$) are highly soluble (over 4 M) due to their higher ionic nature (15, 17). However, both species become insoluble in WiBS electrolyte due to the high lithium salt concentrations. Molecular dynamics (MD) simulations of Li_2S_2 and Li_2S_4 in WiBS electrolyte revealed that these polysulfides severely aggregate, resulting in obvious domain formation in WiBS as shown in Fig. 2 *E* and *F*, with shorter polysulfide yielding more pronounced aggregation. Quantum chemistry calculations predicted higher stability of Li_2S_2 vs. Li_2S_4 in aqueous environment as discussed in *SI Appendix*. Preferential stability of shorter polysulfide Li_2S_2 vs. Li_2S_4 together with their stronger aggregation and separation is consistent with the experimentally observed phase separation of polysulfides in WiBS electrolyte. MD simulations also show that the short-chain Li_2S_x ($x \leq 4$) can indeed extract water molecules from the superconcentrated WiBS electrolyte until reaching equilibrium with WiBS, forming a mixed solid and liquefied anolyte, which is not miscible with the bulk WiBS electrolyte. Hence, the lithiation state of the sulfur anode in WiBS electrolyte should maintain solid–liquid mixed phase, in accordance with the previous electrochemical behavior. Thanks to the immiscibility of saturated Li_2S_x ($x < 4$) anolyte with WiBS electrolyte, the parasitic shuttle reactions of the polysulfides that have been plaguing the nonaqueous Li/S chemistry are effectively suppressed.

X-ray photoelectron spectroscopic (XPS) analysis was also conducted on the S-KB anodes retrieved from the full cells at different SOCs of the third charge (Fig. 2*B*). For clarity, only the $2p_{3/2}$ component of the S $2p_{3/2}/2p_{1/2}$ doublet was analyzed. Because the peaks at the binding energy over 166 eV are dominated by the contributions from LiTFSI and LiOTf salt anion residuals, as demonstrated in *SI Appendix*, Fig. S4, only the spectra in the range of 158–166 eV were selected to fit the S2*p* of S_8, S^0, S^{1-}, and S^{2-} (Fig. 2*B*) (28, 29). At SOC = 0%, only S_8 (164.4 eV) was observed, whereas polysulfide species S_x^{2-} ($8 \geq x \geq 2$) appeared during lithiation, which were fitted with S^0 at 164.0 eV and S^{-1} at 162.2 eV, respectively. In the chain structure of S_x^{2-} species, the two terminal sulfur atoms at both ends bear a formal charge of −1, with several bridging sulfur atoms in the middle bearing a formal charge of zero. The average oxidation states were thus determined by the ratio of terminal/bridging sulfur peaks, leading to an average lithium polysulfide formula approximately equal to Li_2S_6 (SOC = 25%), Li_2S_4 (SOC = 50%), and Li_2S_3 (SOC = 75%), respectively (red line in Fig. 2*C*). Interestingly, the XPS spectra showed that Li_2S, represented by S^{2-} at 160.7 eV, was generated immediately upon lithiation. In the nonaqueous Li–S battery, however, this fully lithiated form would only appear in the very late or even the last stage of lithiation, due to the slow reaction kinetics (6, 20). The early appearance of Li_2S in WiBS electrolyte confirms the rather fast kinetics for the lithiation reactions, and is consistent with a relatively flat charge–discharge profile. At the end of the lithiation (SOC = 100%), Li_2S expectedly becomes the dominant species (72%), in excellent agreement with the 79% of the theoretical capacity obtained previously. Meanwhile, XPS spectra also confirmed the formation of a LiF-rich SEI on anode surface, with a conspicuous change in F 1*s* peaks before and after 20 lithiation cycles. Similar conclusions can be drawn from high-resolution TEM images (*SI Appendix*, Figs. S5 and S6).

In summary, the S-KB composite in WiBS electrolyte seemed to follow a similar lithiation pathway to that in nonaqueous electrolyte, represented by the formation of predominant Li_2S_6, Li_2S_4, Li_2S_2, and Li_2S XPS peaks (8, 30), but with unprecedented fast kinetics. Short-chain LiPS species (Li_2S_x, $x < 6$) have been considered soluble in aqueous media (15), as confirmed by the formation of water-solvated species detected in the Raman spectra for lithium polysulfide. MD simulations also predict that

both solid Li_2S_2 and Li_2S_4 can take very small amount of water from WiBS electrolyte to form solid–liquid mixed semianolyte due to limited free-water in WiBS and large amount of Li_2S_2/Li_2S_4 (*SI Appendix*, Fig. S21). However, using both in situ Raman and mass spectra, we found that only a trace amount of liquid lithium polysulfide (<71 ppm) was observed to diffuse into the bulk electrolyte (*SI Appendix*, Figs. S7 and S8). SEM images and corresponding energy-dispersive X-ray spectroscopy of sulfur demonstrated little change in surface morphology of the S-KB anode (*SI Appendix*, Fig. S9). All these findings, along with the excellent electrochemical behavior, converged to one conclusion that the extremely high concentration of LiTFSI and LiOTf effectively expelled the liquefied short-chain lithium polysulfides from WiBS electrolyte.

In a visual manner, a simple dissolution experiment (Fig. 2*D*) was also carried out to demonstrate the negligible solubility of Li_2S powder and short-chain lithium polysulfide anolyte in WiBS electrolyte. The 4-M aqueous solutions of Li_2S_2 and Li_2S_4 with jacinth color (Fig. 2*D* and *SI Appendix*, Fig. S10*A*) were nominally formed with a 1:1 and 3:1 molar radio of sulfur to Li_2S aqueous solution by the following reaction:

$$Li_2S + S_{x-1} \leftrightarrow Li_2S_x (x < 6) \quad [1]$$

These lithium polysulfide solutions were mixed with a 28-mol·kg^{-1} WiBS electrolyte and allowed to stand for 2 or 24 h, respectively. As shown in Fig. 2*D*, a yellow boundary still existed between the two distinct phases, with the upper part being lithium polysulfide solutions due to their lower densities, and lower part being WiBS bulk electrolyte, as supported by their respective Raman spectra (*SI Appendix*, Fig. S11 *A* and *B*). To prove that such phase separation is thermodynamic, a more rigorous miscibility test was done for longer duration (5 d) at higher temperature (70 °C; *SI Appendix*, Fig. S10*B*) with the same results. Carefully examining the yellow interlayer between the aqueous solution of short-chain lithium polysulfide and WiBS electrolyte in Fig. 2*D*, we detected a cluster of white small solid particles, which had diffused from the yellow phase into the clear electrolyte phase after 24 h. A similar phenomenon was also observed in the full cell after long-term cycling (*SI Appendix*, Fig. S12*A*). These particles were collected by centrifugation and determined with Raman spectroscopy to be elemental sulfur (*SI Appendix*, Fig. S11*C*), which might have been generated from a disproportionation reaction of metastable polysulfides following the reverse direction of Eq. **1**. On both sides of the interface, Li_2S_x and LiTFSI/LiOTf should be nearly saturated, but inevitably cross-over of trace water still occurs at the interface, causing such disproportionation reaction.

Polysulfides dissolved in aqueous solutions have a tendency to hydrolyze rapidly and release hydrosulphide anion HS^- and/or H_2S, which would be hazardous from both battery performance and safety/environment considerations (17). This side reaction was found to be effectively suppressed in WiBS electrolyte system, because of the low activity of water molecules that are tightly bound by the high population of cations and anions. Quantum chemistry calculations also showed that such H-transfer reaction is energetically unfavorable for Li_2S_4 in WiBS, as shown in *SI Appendix*, Figs. S18–S20.

Electrochemical Performance of S-KB/$LiMn_2O_4$ Full Cells. A full cell of the previously unobserved Li^+/S chemistry was constructed using the S-KB anode coupled with a $LiMn_2O_4$ cathode (*SI Appendix*, Fig. S13*A*) in WiBS electrolyte, and its electrochemical behavior was evaluated at different current densities (Fig. 3*A*). The cathode/anode capacity ratio was set at 1.03:1, and the areal sulfur loadings in S-KB anode was set at a high value of ~8 mg·cm^{-2} (31). Remarkably, at a slow rate of 0.2C (discharge/charge of full theoretical capacity in 5 h), the cell being cycled between 2.2 and ~0.5 V exhibited a single discharge plateau with an average voltage of 1.60 V, delivering a discharge capacity of 84.40 mAh·g of total electrode mass (i.e., 1,327 mAh·g^{-1} of sulfur mass) or an areal capacity of 10.6 mAh·cm^{-2}. The energy density was conservatively estimated to be ~135 Wh/(kg of total electrode mass), which represents a marked improvement not only over all conventional aqueous Li-ion systems (<75 Wh·kg^{-1}) (9, 11), but in particular also over what was achieved by the highly concentrated aqueous electrolytes (12, 13, 18). At a rate five times higher (1C), the capacity dropped only slightly, to 68.24 mAh·g^{-1}, reflecting the fast kinetics of the cell reactions.

To examine the reaction kinetics of S-KB anodes, we performed galvanostatic intermittent titration experiments (GITT) (Fig. 3*B*) on an S-KB/$LiMn_2O_4$ full cell with the capacity of the $LiMn_2O_4$ cathode being in excess by five times to that of the S-KB anode. A constant current (0.1C) was applied as short pulses, between which the system was allowed to relax to quasi-equilibrium (*Materials and Methods*). Remarkably, a reversible capacity close to the theoretical value of sulfur (1,667 mAh·g^{-1}) was achieved during the first cycle under this quasi-equilibrium condition, which cannot be achieved in nonaqueous systems (32, 33). Moreover, the gap between the potential at the end of each pulse (polarization potential, as indicated by the black line in Fig. 3*B*) and the potential at the end of each relaxation (quasi-equilibrium potential, as indicated by the red line) were consistently low at 30–80 mV during most of the charge/discharge processes, except at the end of charge/discharge due to the increase in concentration polarization. This remarkably small overpotential further confirms the fast lithiation/delithiation kinetics of the S-KB anode in WiBS electrolyte. In sharp contrast, the lithiation process in typical nonaqueous electrolytes based on 1,3-dioxalane and dimethoxyethane normally undergoes three distinct stages with varying kinetics, which correspond to phase

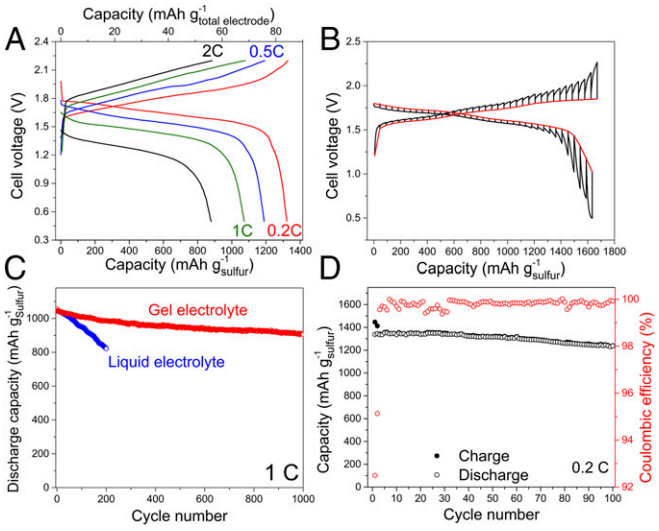

Fig. 3. Electrochemical performance of S-KB/$LiMn_2O_4$ full cells and S-KB cathodes. (*A*) Voltage profiles of full cell with S-KB anode and $LiMn_2O_4$ cathode in WiBS electrolyte at current densities ranging from 0.2 to 2C. The specific capacities were evaluated both by sulfur mass and total electrode (S and $LiMn_2O_4$) mass. (*B*) GITT characterization of S-KB cathode in WiBS electrolyte with five times higher capacity of $LiMn_2O_4$ cathode to avoid the interference by two plateaus of $LiMn_2O_4$. Red curve is quasi-equilibrium potential of sulfur at different lithiation/delithiation stages, which was constructed from the last data point of each open-circuit voltage period. (*C*) Corresponding cycling performance of aqueous S-KB/$LiMn_2O_4$ full cells with liquid and gel electrolytes at 1C rate; and (*D*) cycling stability of S-KB/$LiMn_2O_4$ full cells in aqueous gel electrolyte at low rate of 0.2C. The specific capacities were evaluated by sulfur mass.

changes from solid S_8 to soluble S_x^{2-} species ($x > 4$) followed by isolated solid Li_2S_x ($x = 2$ and 1) (32), accompanied by much higher potential hysteresis. A single-potential plateau similar to this work has been observed in the Li/S cell with a solid-state electrolyte (34), but still with much higher overpotential. The aqueous sulfur chemistry described in this work provides an avenue to exploit this cheap and energy-dense cathode material.

Cycling Performance of S-KB/LMO Full Cells. The cycling stability has always been an issue plaguing nonaqueous Li/S batteries, whose capacity fades rapidly due to the dissolution of polysulfide intermediates and the parasitic shuttling reactions thereafter, which result in self-discharge within the cell as well as continuous loss of active materials (30). However, in the 28-mol·kg^{-1} WiBS electrolyte, they are effectively suppressed because of the very limited free-water in WiBS and the phase separation between polysulfides and WiBS. The full Li-ion/sulfur cell in 28-mol·kg^{-1} WiBS electrolyte showed good cycling stability (Fig. 3*C*) due to the immobilization of the polysulfide species. However, a capacity decay of 22% still occurs over 200 cycles at 1C rate, indicating that the disproportionation reaction of lithium polysulfides still prevailed over the time due to cross-over of trace water at the interface. This side reaction slowly created elemental sulfur particles during repeated charge/discharge, leading to a major loss of active material (*SI Appendix*, Figs. S11*C* and S12*A*).

Further efforts were made to mitigate the generation and cross-over of elemental sulfur particles by immobilizing them in a "solidified" WiBS electrolyte with the formation of a polymeric gel. A hydrophilic polymer polyvinyl alcohol (PVA), which has been widely used as a matrix in solid-state supercapacitors (35, 36), was introduced into the WiBS electrolyte to form a hydrogel (*SI Appendix*, Fig. S14 *A* and *B*). Unexpected high solubility of PVA (mass ratio of PVA to water > 0.8:1) suggested that PVA chain with abundant hydroxyl groups, which also possess solvation power, must have interacted with lithium salts. The FTIR (*SI Appendix*, Fig. S14*C*) of this gel polymer electrolyte (GPE) is almost identical to its parental aqueous electrolyte, and there is also little difference in ion conduction as well as interphasial behavior between the GPE and its parental aqueous electrolyte (*SI Appendix*, Fig. S14*D*), as evidenced by almost identical electrochemical impedance spectroscopy in the course of 50 cycles (*SI Appendix*, Fig. S15). The S-KB/$LiMn_2O_4$ in this 28-mol·kg^{-1} WiBS-GPE exhibited almost identical charge/discharge profiles as that of 28-mol·kg^{-1} WiBS liquid electrolyte (*SI Appendix*, Fig. S14*F*). The hydrophilic polymer matrix, however, is expected to further interact with the lithium salts dissolved in WiBS, and repels the polysulfide anions, providing a chemical barrier to the sulfur loss into the bulk aqueous electrolyte (*SI Appendix*, Fig. S12*B*). With PVA polymer bonding with both water molecule and Li salts, the cross-over of trace water was significantly minimized, and the disproportionation reaction of LiPS essentially eliminated. This approach effectively maintains the sulfur in an active electrochemical state, thus significantly reducing capacity decay to 7% in the first 200 cycles at 1C. More importantly, after 1,000 cycles at 1C, the capacity still retained 86% of its initial value, corresponding to a very small capacity decay of 0.014% per cycle (Fig. 3*C*). This low fading rate is the best observed among all lithium/sulfur batteries, either nonaqueous or aqueous (5, 7). Even at a low charge/discharge rate of 0.2C, which has always been a challenge not only for the Li/S system but for all aqueous systems, the capacity decay was still only 9% after 100 cycles (Fig. 3*D*). During the SEI formation on the anode surface in the initial several cycles, Coulombic efficiency quickly increased from 92.49% in the first cycle, to 95.4% in the second cycle, then to 99.95 at the 30th cycle, and eventually reached ~100% after 40 cycles. Such high Coulombic efficiency ensures the long cycle stability. The effectiveness of this strategy in suppressing the side reaction was also evaluated by measuring the self-discharge rate of a Li^+/S cell at 100% SOC (*SI Appendix*, Fig. S16). As expected, a pronounced increase in retained discharge capacity was observed after a 24-h open-circuit voltage relaxation.

High Energy Density S-KB/HV-$LiCoO_2$ Full Cells. We have already constructed a unique Li^+/S battery based on this unique sulfur chemistry, which, with sulfur coupled with a $LiMn_2O_4$ cathode in WiBS electrolyte, achieved a gravimetric energy density of 135 Wh/(kg of total electrode mass) and a volumetric energy densities of ~384 Wh/(L of total electrode and electrolyte). It should be noted that the energy density of the S-KB/$LiMn_2O_4$ cell is limited by the $LiMn_2O_4$ due to its low potential and moderate capacity. For practical applications where high energy density is desired, cathode candidates with higher specific capacity and redox potential should be further explored (Fig. 4*A*). For instance, high-voltage $LiCoO_2$ (HV-$LiCoO_2$) with a capacity of 170 mAh·g^{-1} (*SI Appendix*, Fig. S13*B*) would make a better cathode in this aqueous sulfur battery (37), raising the energy density to an unprecedentedly high level for aqueous batteries. Indeed, such a full cell based on HV-$LiCoO_2$ cathode and S-KB anode delivered a stable discharge capacity of 119 mAh/(g of total electrode mass) with an average voltage of 1.64 V at 0.2C, leading to a gravimetric energy density of 195 Wh/(kg of total electrode mass) and a volumetric energy densities of ~454 Wh/(L of total electrode and electrolyte volume; Fig. 4*B*). With further optimization and engineering in cell design, the theoretical

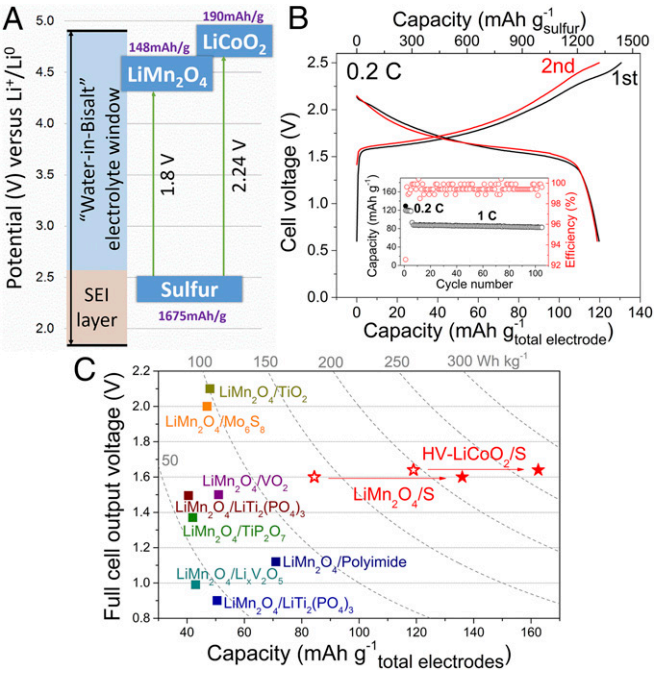

Fig. 4. Energy densities of aqueous Li-ion batteries. (*A*) Illustration of S/$LiMn_2O_4$ and S/HV-$LiCoO_2$ full cell in WiBS electrolyte with expanded electrochemical stability window. (*B*) Voltage profiles of S/HV-$LiCoO_2$ full cell in WiBS GPE at rate of 0.2C. (*Inset*) Capacity stability and coulombic efficiency during cycling. The specific capacities were evaluated by both sulfur mass and total electrode mass. (*C*) Comparisons of theoretical (closed stars) and actual (open stars) voltages, capacities, and energy densities of aqueous Li^+/S batteries with all reported aqueous electrochemical couples (squares). All of the gravimetric capacities and energy densities are based on the total weight of positive and negative electrodes, including the active materials, carbon additives, and binders (electrolyte and cell packaging were not considered). The theoretical material capacities and voltages were used for calculating the theoretical energy densities. The actual energy densities of the $LiMn_2O_4$/S and HV-$LiCoO_2$/S cells were experimentally obtained.

value of 267 Wh·kg^{-1} for the sulfur/HV-$LiCoO_2$ couple (Fig. 4*C*) could be eventually achieved. This highest value of energy density ever achieved in aqueous batteries is already approaching the commercial LIB chemistry (*SI Appendix*, Table S2), along with much superior safety.

As an overview of the state-of-the-art, in Fig. 4*C* we compared our aqueous Li^+/S batteries against other successful aqueous systems reported previously. In most cases, energy densities for aqueous systems were below 78 Wh·kg^{-1} (10, 38–40). The high-voltage aqueous Li-ion systems achieved in WiS electrolyte can deliver higher-energy density between 84 and 101 Wh·kg^{-1} (12, 13), although Yamada et al. (18) raised this value to ~130 Wh·kg^{-1} by coupling lithiated titanate with $LiCoO_2$. Even higher energy density (183 Wh·kg^{-1} based on the weight of active electrode materials) became possible when Zn^{2+} and Li^+ chemistries are hybridized (41). It should be noted that the value of ~200 Wh·kg^{-1} obtained from S/$LiCoO_2$ couple is already higher than some nonaqueous Li-ion batteries, e.g., $LiMn_2O_4$/$Li_4Ti_5O_{12}$ (160 Wh·kg^{-1}).

Conclusion

We demonstrated a unique sulfur chemistry in superconcentrated aqueous electrolyte, which delivers a close-to-theoretical capacity and fast reaction kinetics. We believe that, with the judicious choice of proper cathodes with higher capacities or potentials, the energy densities of the intrinsically safe and green aqueous rechargeable batteries could be further increased, eventually challenging the commercial nonaqueous LIBs (theoretical energy density of 150~400 Wh·kg^{-1}), especially in applications where the needs for safety, low cost, and low toxicity outweigh those for high energy and power densities. Further efforts should be focused on cost reduction of WiBS electrolyte, making the Li-ion/sulfur battery closer to practical applications. The promising approaches might include alternative low-cost salts with the potentials to form similar phase separation, together with optimized cell engineering.

Materials and Methods

S-KB composite was obtained by thermal treatment to incorporate sulfur into the porous matrix. The electrodes were fabricated by compressing the mixture of active material powder, carbon black, and polytetrafluoroethylene (PTFE) on metal grid current collectors. WiBS aqueous electrolytes were prepared by dissolving 21 mol·kg^{-1} LiTFSI and 7 mol·kg^{-1} LiOTf salts in water. Aqueous gel electrolytes were prepared by further dissolving 10 wt % polyvinyl alcohol in the liquid WiBS electrolyte at 95 °C. More details of the materials used and methods followed are provided in *SI Appendix*.

ACKNOWLEDGMENTS. Funding for this work was provided by Department of Energy Advanced Research Projects Agency - Energy Grant DEAR0000389 (to C.W. and K.X.) and National Aeronautics and Space Administration (NASA) through the interagency agreement NND16AA29I (to O.B.).

1. Tarascon JM, Armand M (2001) Issues and challenges facing rechargeable lithium batteries. *Nature* 414:359–367.
2. Larcher D, Tarascon JM (2015) Towards greener and more sustainable batteries for electrical energy storage. *Nat Chem* 7:19–29.
3. Whittingham MS (2004) Lithium batteries and cathode materials. *Chem Rev* 104: 4271–4301.
4. Ji X, Lee KT, Nazar LF (2009) A highly ordered nanostructured carbon-sulphur cathode for lithium-sulphur batteries. *Nat Mater* 8:500–506.
5. Seh ZW, et al. (2014) Two-dimensional layered transition metal disulphides for effective encapsulation of high-capacity lithium sulphide cathodes. *Nat Commun* 5:5017.
6. Su YS, Fu Y, Cochell T, Manthiram A (2013) A strategic approach to recharging lithium-sulphur batteries for long cycle life. *Nat Commun* 4:2985.
7. Seh ZW, et al. (2013) Sulphur-TiO2 yolk-shell nanoarchitecture with internal void space for long-cycle lithium-sulphur batteries. *Nat Commun* 4:1331.
8. Zhang S, Ueno K, Dokko K, Watanabe M (2015) Recent advances in electrolytes for lithium-sulfur batteries. *Adv Energy Mater* 5:1500117.
9. Kim H, et al. (2014) Aqueous rechargeable Li and Na ion batteries. *Chem Rev* 114: 11788–11827.
10. Li W, Dahn JR, Wainwright DS (1994) Rechargeable lithium batteries with aqueous electrolytes. *Science* 264:1115–1118.
11. Wang Y, Yi J, Xia Y (2012) Recent progress in aqueous lithium-ion batteries. *Adv Energy Mater* 2:830–840.
12. Suo L, et al. (2015) "Water-in-salt" electrolyte enables high-voltage aqueous lithium-ion chemistries. *Science* 350:938–943.
13. Suo L, et al. (2016) Advanced high-voltage aqueous lithium-ion battery enabled by "Water-in-Bisalt" electrolyte. *Angew Chem Int Ed Engl* 55:7136–7141.
14. Licht S (1988) Aqueous solubilities, solubility products and standard oxidation-reduction potentials of the metal sulphides. *J Electrochem Soc* 135:2971–2975.
15. Li N, et al. (2014) An aqueous dissolved polysulfide cathode for lithium-sulfur batteries. *Energy Environ Sci* 7:3307–3312.
16. Demir-Cakan R, Morcrette M, Leriche JB, Tarascon JM (2014) An aqueous electrolyte rechargeable Li-ion/polysulfide battery. *J Mater Chem A Mater Energy Sustain* 2:9025–9029.
17. Visco SJ, et al. (2014) US Patent US8828575 B2.
18. Yamada Y, et al. (2016) Hydrate-melt electrolytes for high-energy-density aqueous batteries. *Nat Energy* 1:16129.
19. Jayaprakash N, Shen J, Moganty SS, Corona A, Archer LA (2011) Porous hollow carbon@sulfur composites for high-power lithium-sulfur batteries. *Angew Chem Int Ed Engl* 50:5904–5908.
20. Pang Q, Kundu D, Cuisinier M, Nazar LF (2014) Surface-enhanced redox chemistry of polysulphides on a metallic and polar host for lithium-sulphur batteries. *Nat Commun* 5:4759.
21. Yamin H, Gorenshtein A, Penciner J, Sternberg Y, Peled E (1988) Lithium sulfur battery: oxidation/reduction mechanisms of polysulfides in THF solutions. *J Electrochem Soc* 135:1045–1048.
22. Ji X, Nazar LF (2010) Advances in Li-S batteries. *J Mater Chem* 20:9821–9826.
23. Mikhaylik YV, Akridge JR (2004) Polysulfide shuttle study in the Li/S battery system. *J Electrochem Soc* 151:A1969–A1976.
24. Yeon JT, et al. (2012) Raman spectroscopic and X-ray diffraction studies of sulfur composite electrodes during discharge and charge. *J Electrochem Soc* 159: A1308–A1314.
25. Janz GJ, Coutts JW, Downey JR, Roduner E (1976) Raman studies of sulfur-containing anions in inorganic polysulfides. Potassium polysulfides. *Inorg Chem* 15:1755–1759.
26. Smith LC, et al. (2016) Sol–gel encapsulated lithium polysulfide catholyte and its application in lithium–sulfur batteries. *Mater Horiz* 3:137–144.
27. Wu HL, Huff LA, Gewirth AA (2015) In situ Raman spectroscopy of sulfur speciation in lithium-sulfur batteries. *ACS Appl Mater Interfaces* 7:1709–1719.
28. Fantauzzi M, Elsener B, Atzei D, Rigoldi A, Rossi A (2015) Exploiting XPS for the identification of sulphides and polysulfides. *RSC Advances* 5:75953–75963.
29. Helen M, et al. (2015) Single step transformation of sulphur to Li2S2/Li2S in Li-S batteries. *Sci Rep* 5:12146.
30. Bruce PG, Freunberger SA, Hardwick LJ, Tarascon JM (2011) Li-O_2 and Li-S batteries with high energy storage. *Nat Mater* 11:19–29.
31. Qie L, Zu C, Manthiram A (2016) A high energy lithium-sulfur battery with ultrahigh-loading lithium polysulfide cathode and its failure mechanism. *Adv Energy Mater* 6:1502459.
32. Busche MR, et al. (2014) Systematical electrochemical study on the parasitic shuttle-effect in lithium-sulfur-cells at different temperatures and different rates. *J Power Sources* 259:289–299.
33. Park J-W, et al. (2013) Solvent effect of room temperature ionic liquids on electrochemical reactions in lithium-sulfur batteries. *J Phys Chem C* 117:4431–4440.
34. Cuisinier M, et al. (2014) Unique behaviour of nonsolvents for polysulfides in lithium–sulfur batteries. *Energy Environ Sci* 7:2697–2705.
35. Peng X, et al. (2016) A zwitterionic gel electrolyte for efficient solid-state supercapacitors. *Nat Commun* 7:11782.
36. Wu C, et al. (2013) Two-dimensional vanadyl phosphate ultrathin nanosheets for high energy density and flexible pseudocapacitors. *Nat Commun* 4:2431.
37. Chen Z, Dahn JR (2004) Methods to obtain excellent capacity retention in $LiCoO_2$ cycled to 4.5 V. *Electrochim Acta* 49:1079–1090.
38. Wang H, Huang K, Zeng Y, Yang S, Chen L (2007) Electrochemical properties of TiP_2O_7 and $LiTi_2(PO_4)_3$ as anode material for lithium ion battery with aqueous solution electrolyte. *Electrochim Acta* 52:3280–3285.
39. Wang H, Zeng Y, Huang K, Liu S, Chen L (2007) Improvement of cycle performance of lithium ion cell $LiMn_2O_4$/$Li_xV_2O_5$ with aqueous solution electrolyte by polypyrrole coating on anode. *Electrochim Acta* 52:5102–5107.
40. Luo JY, Cui WJ, He P, Xia YY (2010) Raising the cycling stability of aqueous lithium-ion batteries by eliminating oxygen in the electrolyte. *Nat Chem* 2:760–765.
41. Zhao J, et al. (2016) High-voltage Zn/$LiMn_{0.8}Fe_{0.2}PO_4$ aqueous rechargeable battery by virtue of "water-in-salt" electrolyte. *Electrochem Commun* 69:6–10.

Supporting Information

Preparation of electrodes and electrolyte. S-KB composite was obtained by homogenously mixing sulfur powder (99.99%, Sigma-Aldrich) and Ketjenblack carbon black (KB, AkzoNobel) and applying a simple heat treatment (155°C), which incorporate sulfur into the porous matrix by melt diffusion. The mass radio of S and KB was 5:4. Composite S-KB anodes were fabricated by compressing S-KB composite and poly(vinylidenedifluoride) (PTFE) at a weight ratio of 9:1 on an aluminum mesh (200 mesh). The areal loading of sulfur was ~8 mg cm^{-2}. Composite $LiMn_2O_4$ and HV-$LiCoO_2$ cathodes were fabricated by compressing active material powder (MTI Corporation), carbon black, and PTFE at weight ratio of 8:1:1 on a stainless steel grid. The aqueous electrolytes were prepared by dissolving 21 mol kg^{-1} LiTFSI (>98%, TCI Co., Ltd.) in water (HPLC grade), in which an additional 7 mol kg^{-1} LiOTf (>99.996%, Sigma-Aldrich) was dissolved to make the water-in-bisalt electrolyte. Aqueous gel electrolytes were prepared by adding 10 wt.% polyvinyl alcohol (PVA, Sigma-Aldrich) in the liquid water-in-bisalt electrolyte and heated at 95 ° C for 5 h under vigorous stirring. Prior to cell assembly, electrodes and the separator were soaked with the hot gel and then allowed to solidify at room temperature for 10 h.

Electrochemical measurements. The aqueous three-electrode devices for both anode and cathode materials consist of the test material as working electrode, active carbon (about 20 times mass of working) as the counter electrode, Ag/AgCl as the reference electrode, and WiBS solution (21 mol kg^{-1} LiTFSI + 7 mol kg^{-1} LiOTf) as electrolyte. The "m" is molality standing for mol-salt in Kg-solvent. The potential was converted into a scale against Li reference for convenience of comparison. The reference non-aqueous Li/S half cells were assembled in a CR2032-type coin cell using the same S-KB electrode as the cathode, lithium foil as the anode, and a typical electrolyte of 1M LiTFSI in 1,2-dimethoxyethane/1,3-dioxolane (DME/DOL, 1:1 vol%) and 2 wt% $LiNO_3$. Cyclic voltammetry was carried out using a CHI 600E electrochemical work station. The Li-ion/S full cell was assembled as a CR2032-type coin cell using either $LiMn_2O_4$ or $LiCoO_2$ as the cathode, S-KB as the anode, and glass fiber as the separator.

The cathode/anode mass ratios were set at 6.90:1 for S/$LiMn_2O_4$ cell and 4.51:1 for S/$LiCoO_2$ cell. The cells were cycled galvanostatically on a Land BT2000 battery test system (Wuhan, China) at room temperature. The GITT experiment was performed in a two-electrode full cell, with the capacity of the $LiMn_2O_4$ cathode being five times that of the anode to avoid the interference from its two plateaus. The cycling protocol consists in 0.1C current pulses for 10 min alternated with 60 min OCV periods.

Characterization. *In-situ* Raman spectra were collected with a Horiba Jobin Yvon Labram Aramis using a HeNe laser (632.8 nm) between 700 and 60 cm^{-1}. For this characterization, a $LiMn_2O_4$/S full cell was assembled in a well-sealed quartz tube and connected to a galvanostatic battery test system. X-ray photoelectron spectroscopic (XPS) analysis was performed with a high resolution Kratos AXIS 165 X-ray photoelectron spectrometer using monochromic AlKα radiation. Scanning electron microscopy (SEM) of the anode was performed in a Hitachi S-4700 operating at 5 kV. Transmission electron microscopy (TEM) were conducted on a JEOL (Japan) 2100F field emission. The tested S-KB anodes were retrieved from the full cells at different SOCs, then soaked in DME for 1 min to remove most of residual electrolyte. The anion spices were characterized with electrospray ionization time of flight mass spectrometry (AccuTOF, JEOL, USA, Inc.). Mass spectra were acquired under negative mode in *m/z* ranging from 12 to 250 with following parameters: capillary voltage, 2100V; orifice 1 voltage, 20V; orifice 2 voltage, 5V; ring voltage, 5V; dissolution temperature 100oC.

Molecular Dynamics Simulations. Molecular dynamics (MD) simulations were performed on 4m Li_2S_2 or Li_2S_4 dissolved in WiBS aqueous electrolyte (21 mol kg^{-1} LiTFSI +7 mol kg^{-1} LiOTf) at 333 K utilizing many-body polarizable force field as discussed in details as below.

Supplementary figures and tables for the experimental part:

Figures S1 – S16 and Tables S1 – S2

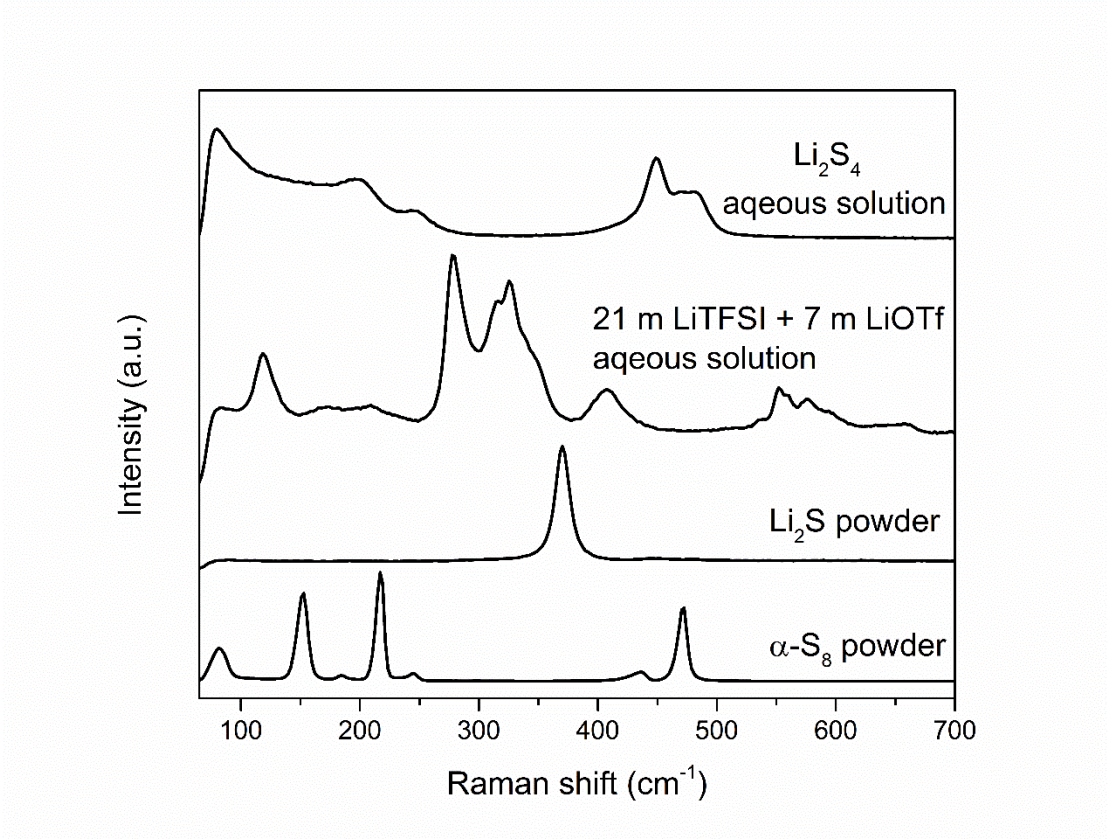

Figure S1. Raman spectra of elemental sulfur powder, Li_2S powder, electrolyte, and Li_2S_4 aqueous solution.

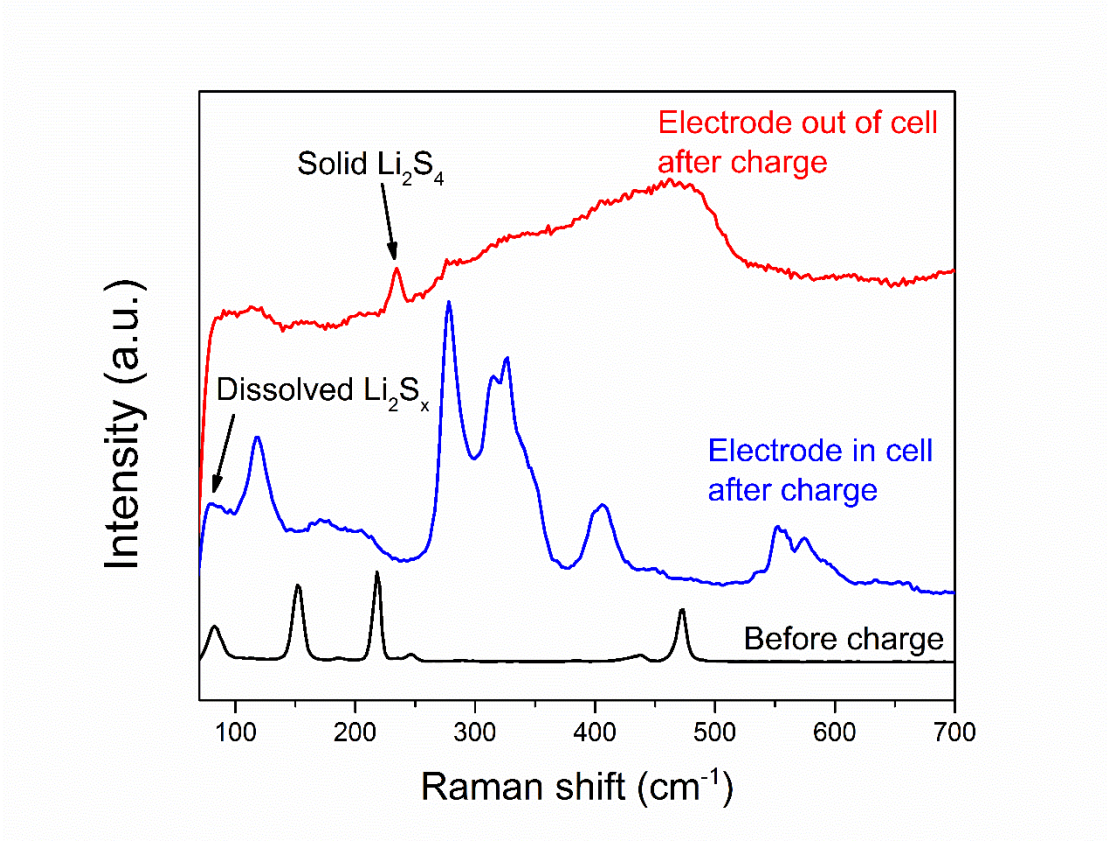

Figure S2. Raman spectra of sulfur anode with elemental sulfur dip-coated aluminum mesh as anode in full cell before and after being charged at the rate of 0.2 C. Before charge, the Raman spectra of S@Al electrode showed only the signal of elemental sulfur. After charge in the cell, the signal of elemental sulfur on S@Al electrode in the cell disappeared along with the appearance of dissolved polysulfide. However, after taking electrode the charged S@Al out of electrolyte and washing with DME, the Raman spectra of electrode showed trace of solid short-chain polysulfide.

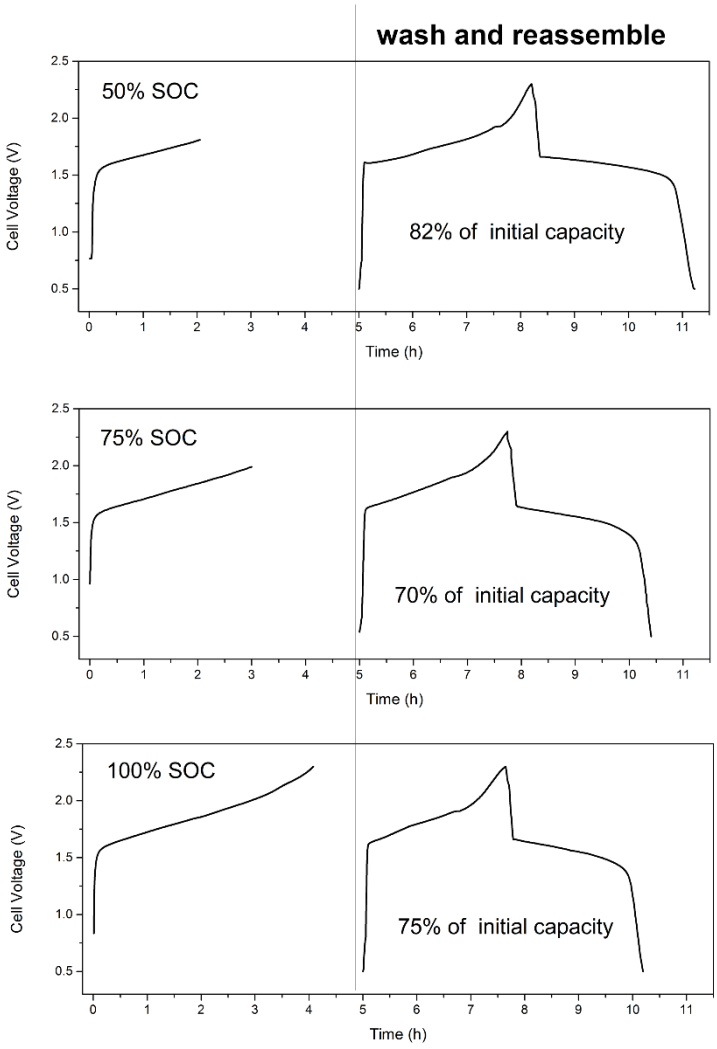

Figure S3. The voltage profiles of S-KB and $LiMn_2O_4$ full cell before and after reassembling. Firstly, the cells were charged to different state of charge (SOC) in WiBS electrolyte. Then the S-KB electrodes were taken out and washed by anhydrous DME for several times. DME was known as a low solubility solvent for short-chain LiPS. After washing, all liquid phase LiPS should be removed. The new cells with these electrodes were reassembled with fresh WiBS electrolyte, fully discharged and tested for new cycles at same current again. The new voltage profiles were similar with the initial ones, with > 70% of initial capacities remaining. This is a clear evident for solid-liquid mixed phase of LiPS, most of which is in solid phase.

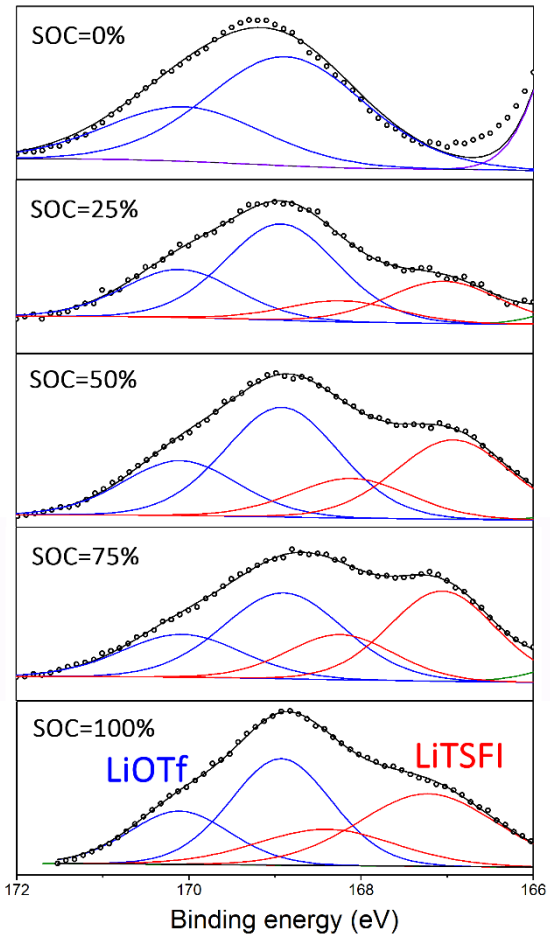

Figure S4. *Ex-situ* XPS S 2*p* spectra of S/KB anode with the binding energy over 166 eV in full cell after charge to specific states. Black dotted lines are experimental data, black lines are overall fitted data, and solid lines in other colors are fitted individual environments in salt anions: $2p_{3/2\text{-blue}}$(LiOTf) 168.9 eV and $2p_{3/2\text{-red}}$(LiTFSI) 167.2 eV.

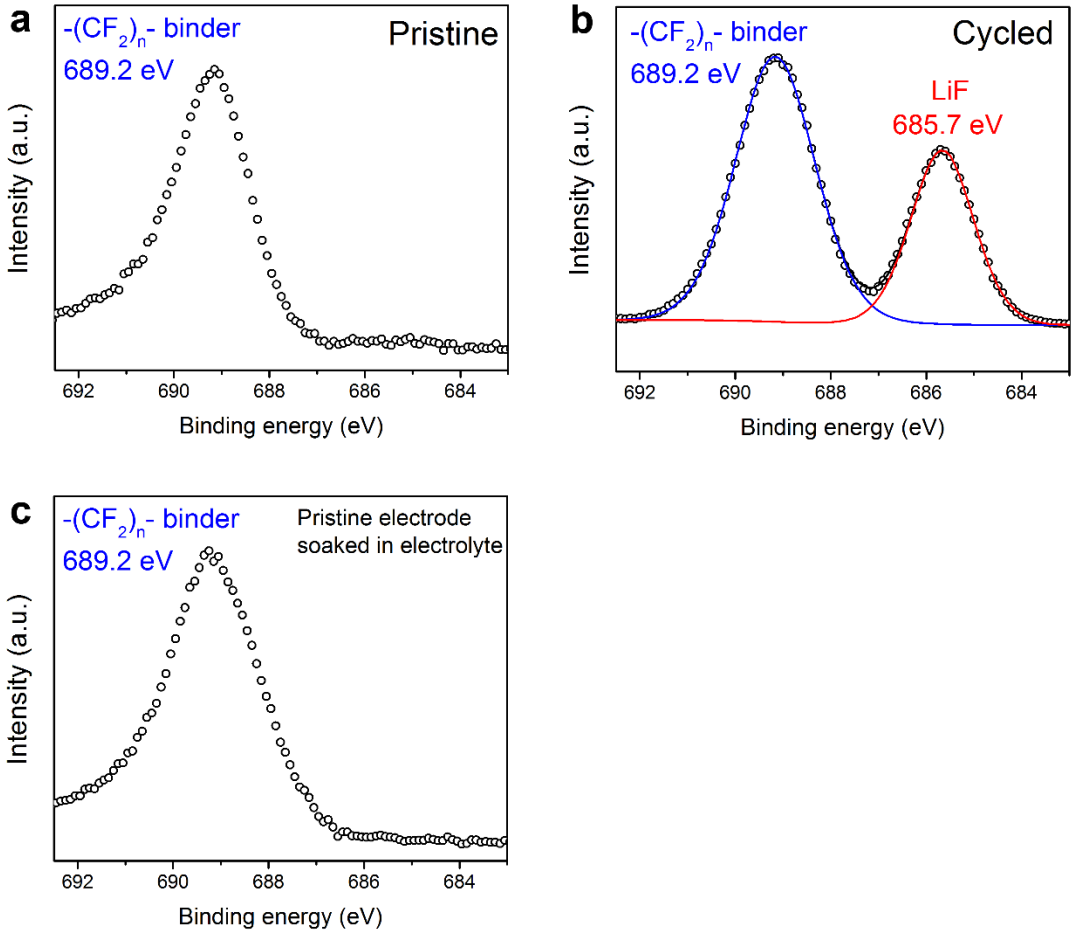

Figure S5. *Ex-situ* XPS F 1*s* spectra of S/KB anode in full cell (a) before and (b) after 20 cycles. (c) A pristine anode as control group was soaked in WiBS electrolyte without cycling. Black dotted lines are experimental data, and solid lines in other colors are fitted individual environments: -$(CF_2)_n$- 689.2 eV and LiF 685.7 eV. The pristine anode only showed a single peak at 689.5 eV, resulting from the poly(tetrafluoroethylene) (PTFE) used as binder in the composite electrode. After three full lithiation cycles, an additional peak of F 1*s* at 685.7 eV corresponding to F^- in LiF was detected, indicating that a LiF-rich interphase has been formed and covered the S-KB composite surface, which serves as an electron barrier and prevents the reduction of water while allowing Li^+ migration (13, 14). The possibility that LiF is created by X-ray irradiation as an artifact was ruled out by a control experiment, where a pristine anode soaked in WiBS electrolyte without cycling generated an XPS spectrum in absence of the 685.7 eV peak (Fig. S5c).

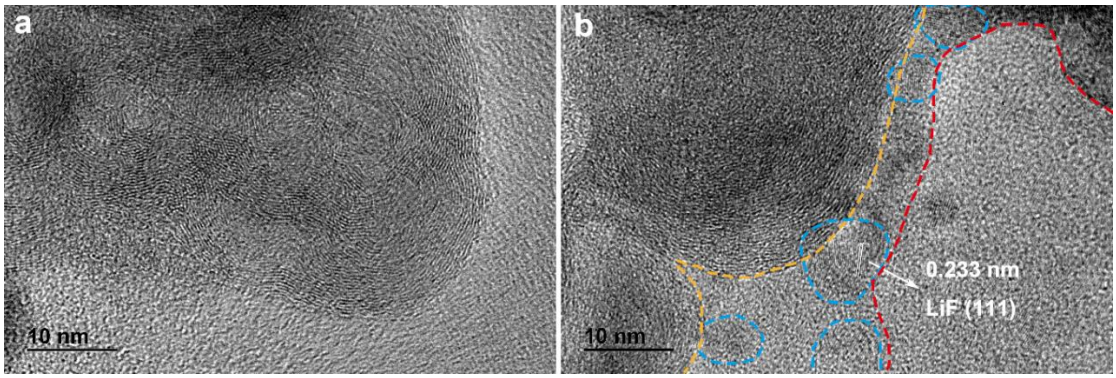

Figure S6. High-resolution TEM images of S-KB (a) before and (b) after 20 cycles at 0.2 C. Yellow and red dash lines denoted outer and inner edge of SEI layer, dotted circles marked the crystal domain of SEI in anode surface. The KB showed a typical onion-like lattice pattern with clear edges before cycling. After 20 cycles at 0.2 C, TEM clearly imaged that KB was entirely covered by a layer of numerous nano-LiF particles that would constitute a uniform SEI of 5–10 nm thick. The isolated nano-sized crystalline particles show the interplanar space of ~ 0.233 nm, which is attributed to (111) interplanar spacing of LiF.

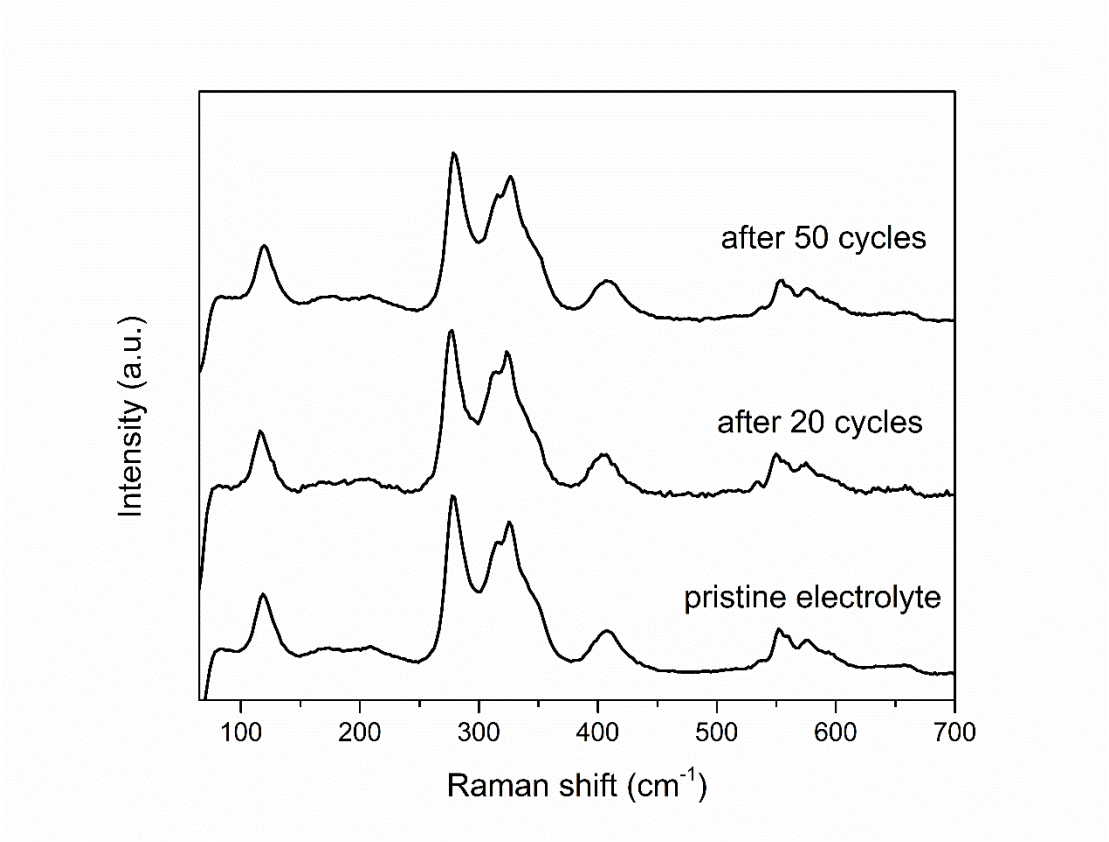

Figure S7. *In-situ* Raman spectra of 21 mol kg^{-1} LiTFSI + 7 mol kg^{-1} LiOTf aqueous solution (WiBS electrolyte) in full cell before and after 20 and 50 cycles at the rate of 0.5C.

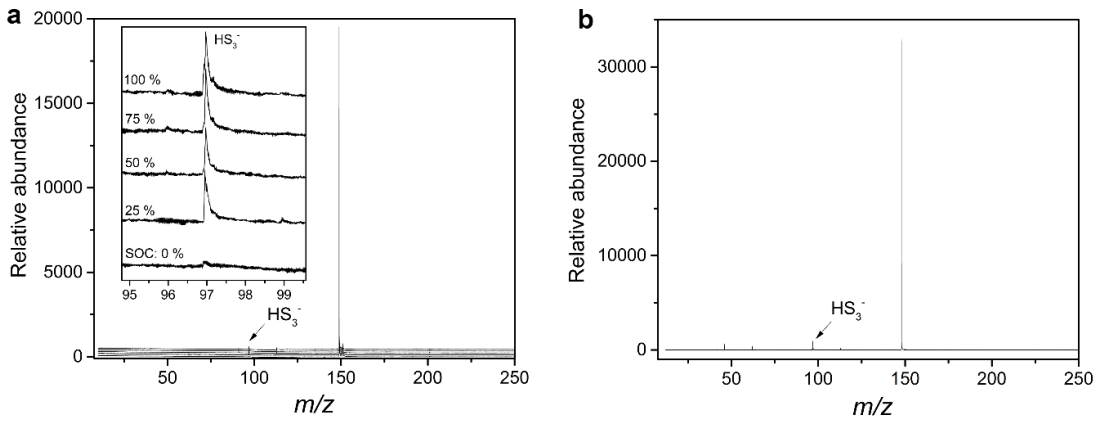

Figure S8. (a) Mass spectra of the electrolyte recovered from the cells which were charged to the different SOC at 0.1 C and then diluted by50 times. According to calculated *m/z* values of all possible sulfur species which might exist in aqueous solution (Table S1), only one peak (*m/z* = 64.95) was identified to be HS_3^- species, appearing in all the electrolyte samples from charged cells. (b) Mass spectrum of 10 μM Li_2S_4 dissolved in WiBS electrolyte diluted by 50 times as a control. The ratio of HS_3^- to the main peak in charged cell is smaller the one in the control sample, indicating that the solubility of sulfur species (only HS_3^-) in the WiBS electrolyte during cycling is < 0.5 mM (~ 71 ppm). It serves as another solid evidence that the reaction intermediate polysulfides are immiscible with the WiBS electrolyte. One additional interesting finding is that, even in WiBS electrolyte diluted by 50 times (~ 0.28 M of LiTFSI and LiOTf), the solubility of Li_2S_4 is still as low as 5 mM, as compared with the high solubility (> 4M) of Li_2S_4 in neat water.

Table S1. Calculated *m/z* values of all possible sulfur species which might exist in aqueous solution.

Species	***m/z***	**Species**	***m/z***	**Species**	***m/z***
S^{2-}	15.98604	HS^-	32.97990	LiS^-	37.98719
S_2^{2-}	31.97207	HS_2^-	64.95197	LiS_2^-	69.95923
S_3^{2-}	47.95811	HS_3^-	96.92404	LiS_3^-	101.93133
S_4^{2-}	63.94414	HS_4^-	128.89611	LiS_4^-	133.90341
S_5^{2-}	79.93018	HS_5^-	160.86818	LiS_5^-	165.87548
$S_3^{\cdot-}$,S_6^{2-}	95.91621	HS_6^-	192.84025	LiS_6^-	197.84755
S_7^{2-}	111.90225	HS_7^-	224.81232	LiS_7^-	229.81962
S_8^{2-}	127.88828	HS_8^-	256.78439	LiS_8^-	261.79169

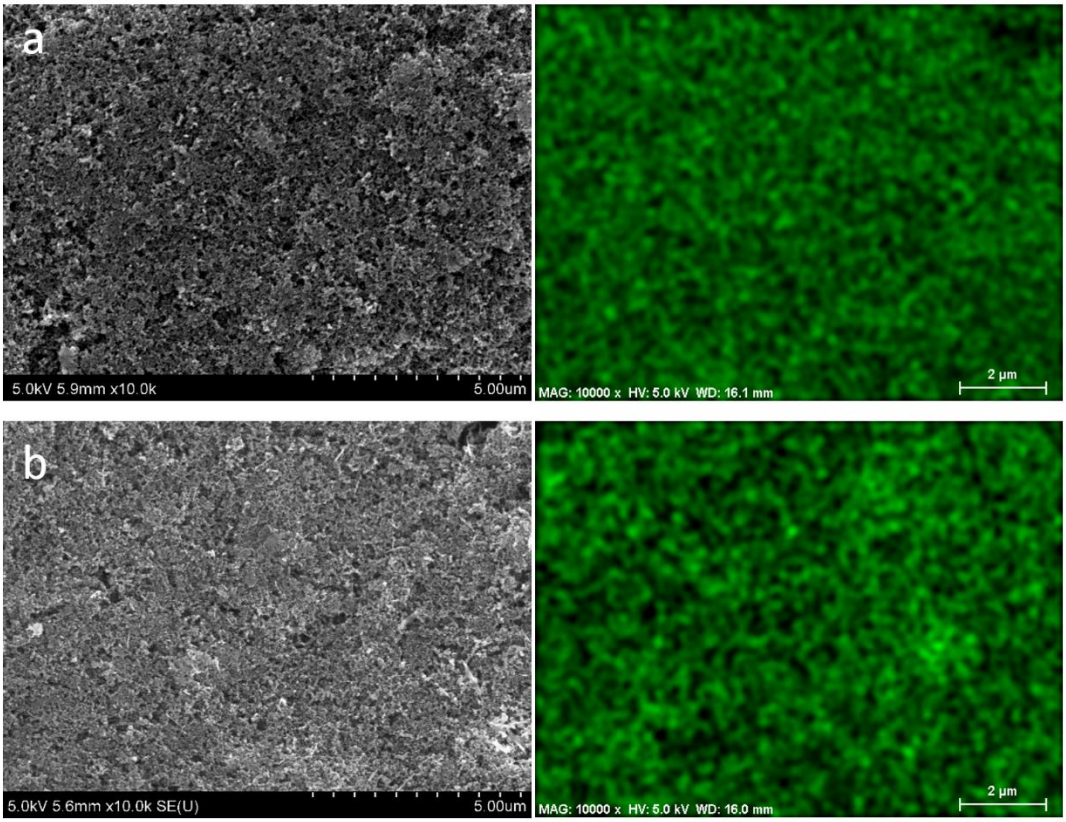

Figure S9. SEM images of S/KB anode (left) and energy-dispersive X-ray spectroscopy (EDX) analysis of sulfur (green) after (a) 1st charge and (b) 20th charge at the rate of 0.5C.

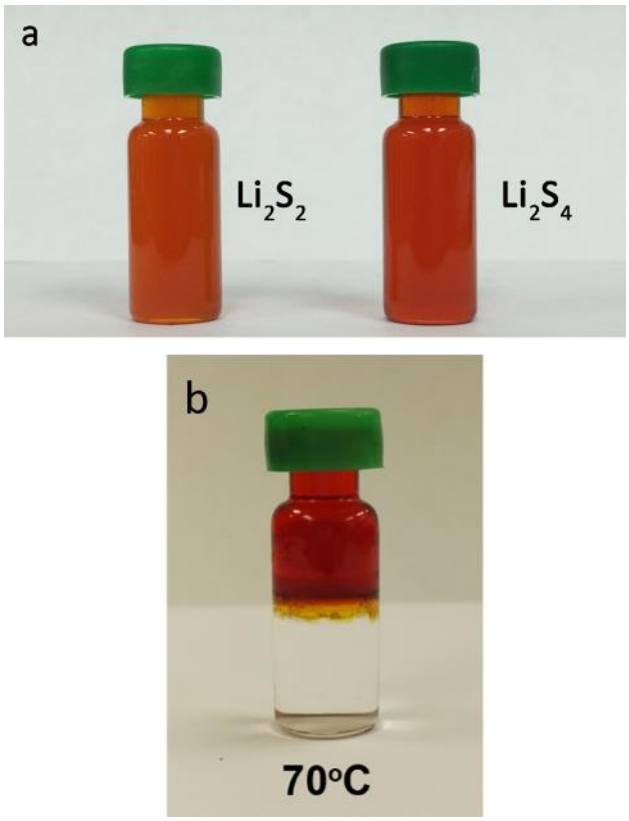

Figure S10. Photos of (a) 4m Li_2S_2 and Li_2S_4 aqueous solutions. (b) Visual observation of the insolubilities for short-chain LiPS (Li_2S_4) in WiBS electrolyte at 70 °C for 5 days, respectively.

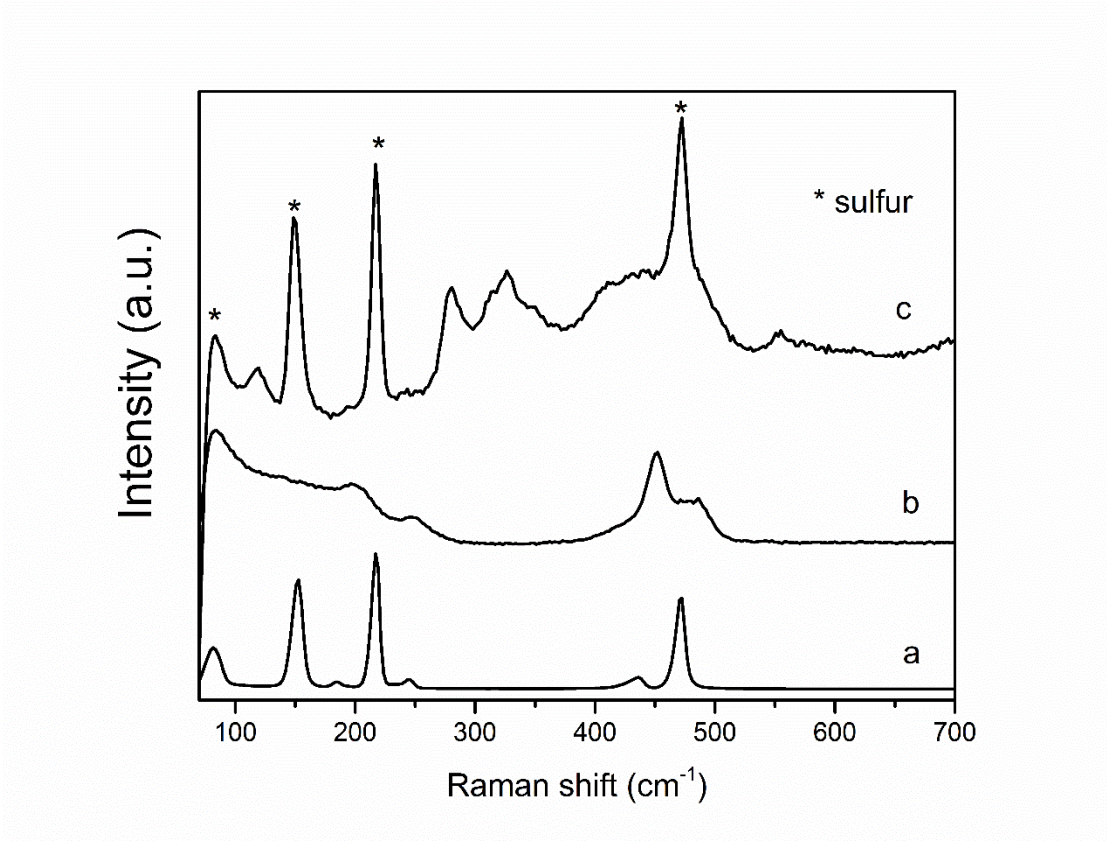

Figure S11. Raman spectra for (a) the bottom part (clear solution) and (b) the top part (jacinth color) in the mixture solution of LiPS solution and 21 mol kg^{-1} LiTFSI + 7 mol kg^{-1} LiOTf electrolyte in Fig. 2d, and (c) the solid white particles diffused into the bottom part of the mixture of LiPS solution and 21 mol kg^{-1} LiTFSI + 7 mol kg^{-1} LiOTf electrolyte. The peaks marked by stars were determined as elemental S_8.

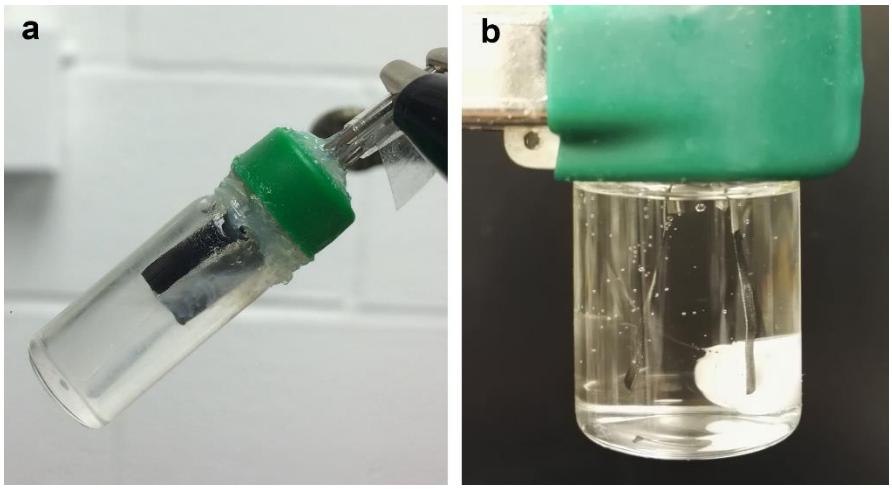

Figure S12. Photos of an S-KB and $LiMn_2O_4$ full cell assembled in a quartz bottle with (a) liquid WiBS electrolyte and (b) WiBS GPE after 200 cycles at 0.5C. A cluster of white small solid particles diffusing into the electrolyte is clearly shown in cell (a). However, no trace of solid particles showed in GPE in cell (b). A few air bubbles were trapped in GPE during assembling of cell (b).

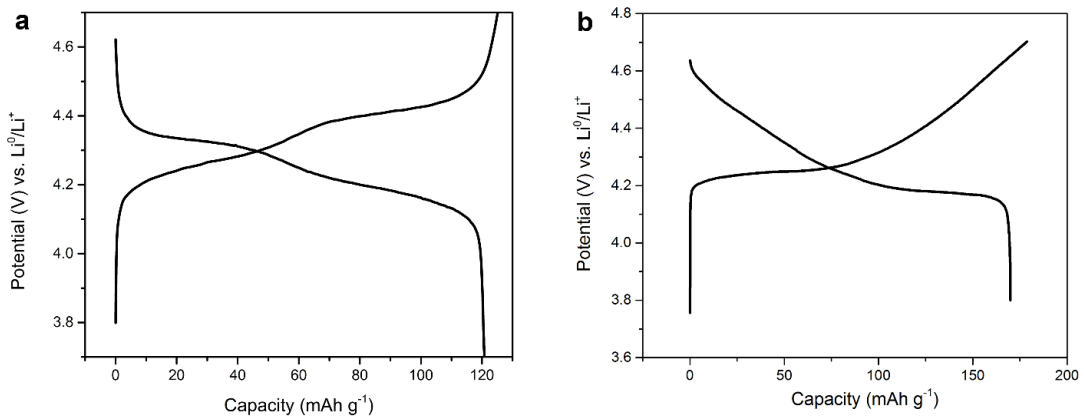

Figure S13. Typical voltage profiles of (a) $LiMn_2O_4$ and (b) HV-$LiCoO_2$ at constant current (0.2C) in 21 mol kg^{-1} LiTFSI + 7 mol kg^{-1} LiOTf solution as aqueous electrolyte. Collected in a three-electrode device with sulfur/carbon composite as working electrodes, and Ag/AgCl as reference electrode. The specific capacities are based on the mass of active materials.

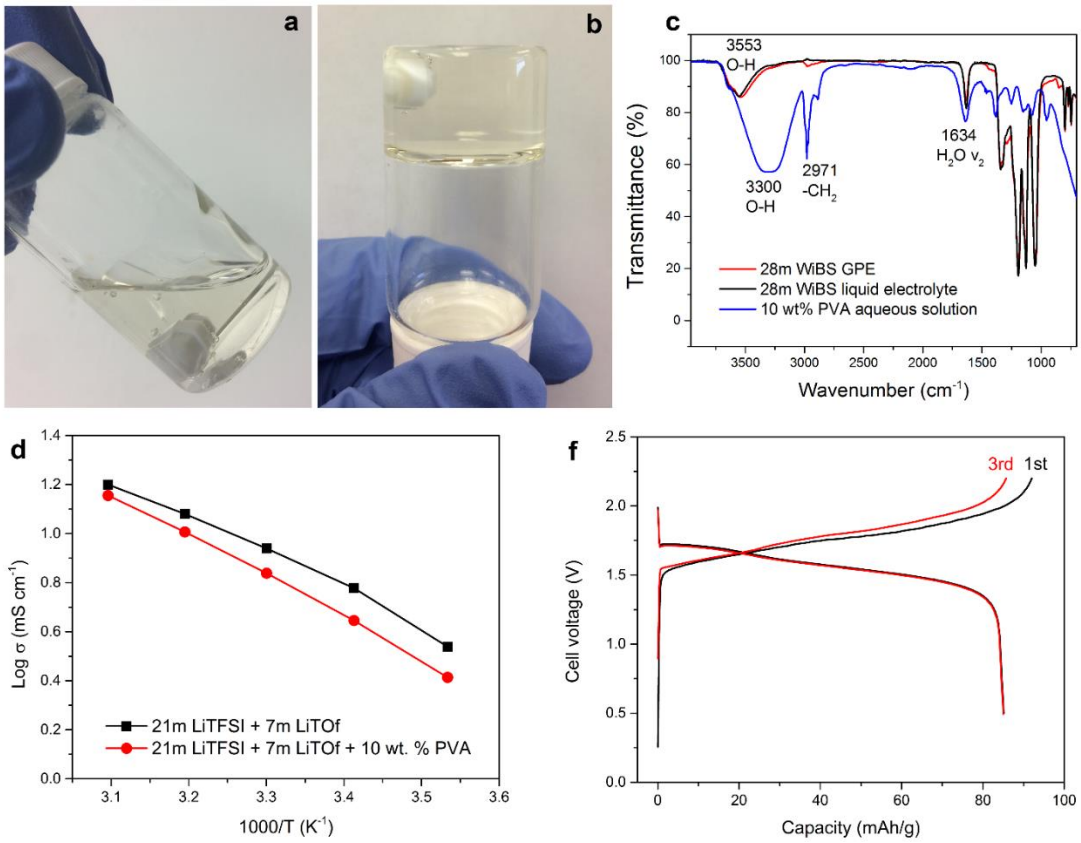

Figure S14. Photos of the transparent WiBS GPE (a) at 95°C (being taken out from oil bath) and (b) at room temperature. (c) Fourier transformed infrared spectroscopy (FTIR) of 28 mol kg^{-1} WiBS GPE, 28 mol kg^{-1} WiBS liquid electrolyte and 10 wt% PVA aqueous solution. (d) Arrhenius plots of lithium ion conductivity (σ) for WiBS liquid electrolyte and GPE in temperature range of 10°C ~ 50°C. (f) Voltage profiles of full cell with S-KB anode and $LiMn_2O_4$ cathode in WiBS GPE at current densities of 0.2C.

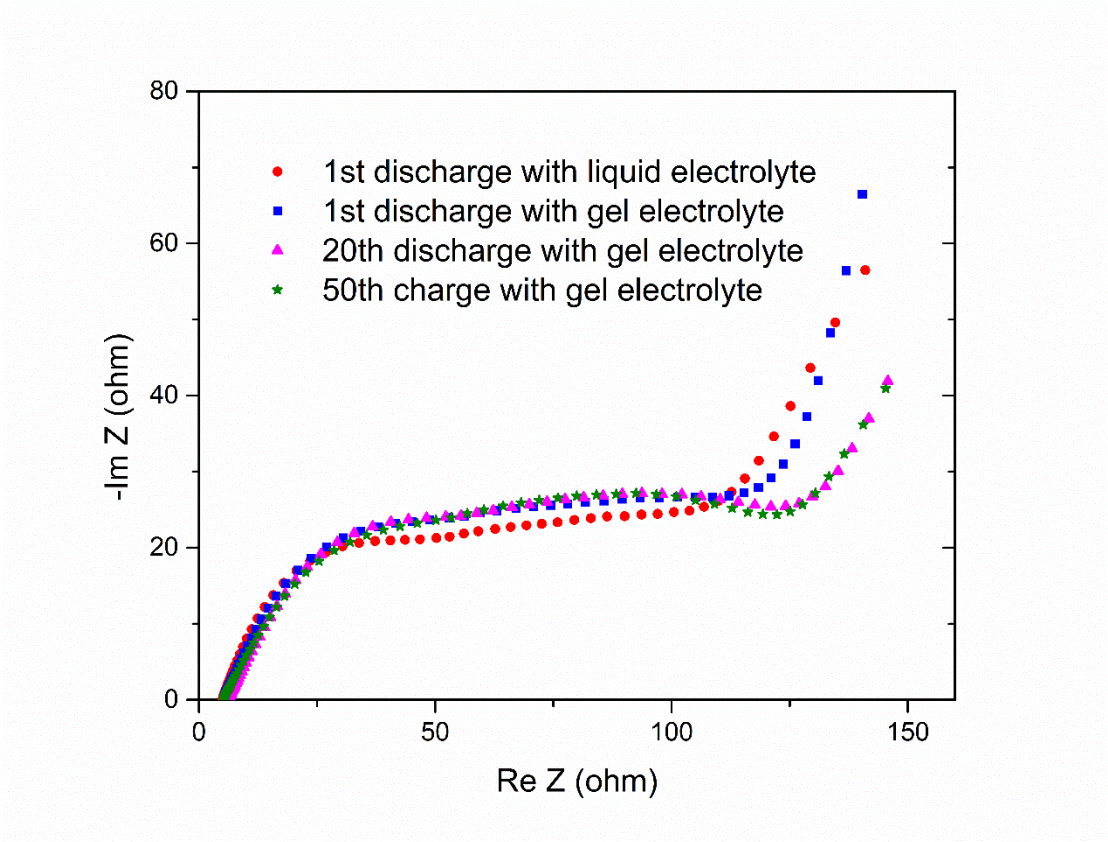

Figure S15. Electrochemical impedance spectroscopy (EIS) of S-KB/$LiMn_2O_4$ full cell with liquid and gel electrolytes at different cycles at 0.5C.

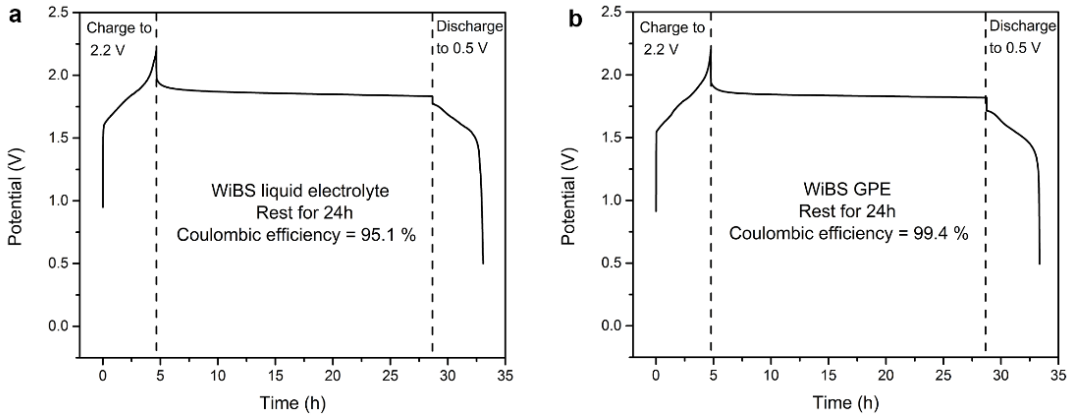

Figure S16. The OCV decays in 24-hour rest of the full cells with the (a) liquid and (b) gel electrolyte at fully charged state of 2.2 V at 0.2C, respectively. The self-discharge was evaluated by comparison with the columbic efficiency and the capacity loss after resting.

Table S2. Comparisons of aqueous Li-ion/S batteries with modern commercial Li-ion battery. The energy density calculations were based on the theoretical specific capacities of active materials.

	$LiCoO_2$/graphite	HV-$LiCoO_2$/S-KB (this work)			
Electrolyte	flammable carbonate base	aqueous			
Cell voltage	3.7 V	1.64 V			
Anode carbon ratio		70 %	50 %	30 %	0 %
Energy density (Wh/kg)	376	220	245	257	267

Calculation details:

Theoretical specific capacities:

$LiCoO_2$: 140 mAh/g

Graphite: 372 mAh/g

HV-$LiCoO_2$: 180 mAh/g

Sulfur: 1675 mAh/g

The energy density of electrochemical couples:

$LiCoO_2$/Graphite: 3.7 V × 1/ (1/140 mAh/g +1/372 mAh/g) = 376 Wh/Kg

HV-$LiCoO_2$/S-KB (70 % carbon): 1.64 V × 1/ (1/180 mAh/g +1/503 mAh/g) = 217 Wh/Kg

HV-$LiCoO_2$/S-KB (0 % carbon): 1.64 V × 1/ (1/180 mAh/g +1/1675 mAh/g) = 267 Wh/Kg

Quantum Chemistry Study of Lithium Polysulfide Protonation and Lithium Dissociation

Strategies for selecting electrolytes to limit polysulfide solubility have been recently reviewed (1), outlining the design rules for maximizing solubility of the supporting salt (e.g. LiTFSI, $LiCF_3SO_3$) and minimizing lithium polysulfide. The suggested strategies fall largely within two categories: a) limited solvent and b) selective solvent design to achieve sparingly solvating electrolytes. In the case of aqueous electrolytes the solvent is specified, it is water. Thus, the solvent limitation strategy is pursued (2, 3) together with the anode coating by SEI. Weakly associating [with Li^+] anions such as bis(trifluoromethane)sulfonamide ($TFSI^-$) or bis(fluorosulfonyl)imide (FSI^-) preferentially dissociate over lithium polysulfide s and were shown to result in the reduced polysulfide solubility in concentrated electrolytes (4). The gas-phase cation-anion binding energy is an often used approximate marker for the salt dissociation (5, 6). We first discuss the relative binding energies of the Li_2S_2, Li_2S_4, LiTFSI and $LiCF_3SO_3$ salts in gas-phase and follow up with the more rigorous study of the free energy for the Li^+ cation dissociation using a cluster – continuum approach that takes into account solvent effects. The later are introduced by explicitly including the solvent molecules immediately interacting with the anion or lithium as well as the polarized continuum model (PCM) to account for water that was not included explicitly. The PCM model using water parameters was used in all calculations as implemented in Gaussian g09 (revision c) package unless stated otherwise (7).

In gas-phase the Li^+ binding energy to the $TFSI^-$ anion is around -135 kcal/mol (-5.88 eV) (8), which is much lower than the first Li^+ dissociation energy for Li_2S_4 of -148.8 kcal/mol (-6.45 eV) and second lithium dissociation energy of -253.0 kcal/mol (-10.97 eV) obtained from G4MP2 quantum chemistry (QC) calculations relative to the singlet states of LiS_2^- and $S_2^{(2-)}$ as shown in Fig. S17. The first Li^+ dissociation energy from Li_2S_2 is even higher that the Li_2S_4 dissociation energy. It is -161.9 kcal/mol from G4MP2 calculations in gas-phase, suggesting the preferential dissociation of the LiTFSI salt compared to Li_2S_4 polysufide and especially Li_2S_2. The lithium binding energy in $LiCF_3SO_3$ is -138.6 kcal/mol (-6.01 eV) at G4MP2 level (9), which is higher than the binding energy in LiTFSI but still much lower than the binding energy in Li_2S_2 or Li_2S_4.

$\Delta E(Li_2S \rightarrow LiS^- + Li^+)$
G4MP2 -166.1
MP2/Tz -167.9
FF -167.1

$\Delta E(Li_2S_2 \rightarrow LiS_2^- + Li^+)$
G4MP2 -161.9
MP2/Tz -163.2
FF -162.3

$\Delta E(Li_2S_4 \rightarrow LiS_4^- + Li^+)$
G4MP2 -148.8
MP2/Tz -150.1
FF -151.1

$\Delta E(LiS_4^- \rightarrow S_4^{2-} + Li^+)$
G4MP2 -253
FF -253.4

Figure S17. The Li^+ binding energies for the Li_2S_x clusters from quantum chemistry calculations using G4MP2, Møller–Plesset perturbation theory (MP2)/aug-cc-pvTz (denoted as MP2/Tz) methods and molecular mechanics using developed force field (denoted FF) in kcal/mol.

Next, the Li^+ cation dissociation from sulfide s was examined for the representative Li_2S_x –based (x=1, 2, 4) sulfide complexes using a cluster – continuum approach. The PBE/6-31+G(d,p) density functional theory method and G4MP2 were used as implemented in g09 Gaussian package. PBE functional was chosen as it was found to adequately describe Li-solvent binding energy (10) and is significantly less computationally expensive than the more accurate G4MP2 composite methodology that was also utilized.

We begin by examining Li_2S_2-$(H_2O)_6$ clusters immersed in implicit solvent modelled via PCM(water) and focus on the energetics of the Li^+ cation dissociation and proton transfer to anion as a result of water coordination. The relative binding energies from G4MP2 and PBE/6-31+G(d,p) calculations are shown in Fig. S18. The following scenarios were investigated: 1) an anion associated with the Li^+ and H^+ cations (LiS_2H: complex-a); 2) an anion associated with Li^+ but not H^+ (LiS_2: complexes b-c); 3) an anion that is solvent separated from the Li^+ cation and H^+ ($S_2^{(2-)}$: complexes d-f) and 4) the anion associated only with protons but solvent separated from Li^+ (S_2H: complexes g-h). QC calculations show that the LiS_2^- complexes (b-c) tend to be slightly less stable than the S_2^- anions with the Li^+ cations separated by water molecules (complexes d-f). The later complexes are among the most stable solvates. These results indicate that the Li_2S_2 salt in water is likely to be have a significant fraction of anions with both Li^+ dissociated from it when a sufficient amount of free water is available. Excess water is also going to result in water decomposition and LiS_2H and HS_2^- formation as evident from the high relative stability of complexes (a) and (g). The S_2H^- complexes (g-h) are slightly less stable than the complexes where S_2^{2-} is formed. Based upon

QC calculations, stability of the Li_2S_2-based solvates could be approximated as follows: $S_2^{2-} \approx S_2H^- > LiS_2H > LiS_2$. We conclude that when free water is available, both Li^+ cations are likely to dissociate from Li_2S_2, while the S_2H^- and LiS_2H solvates are also expected to be present.

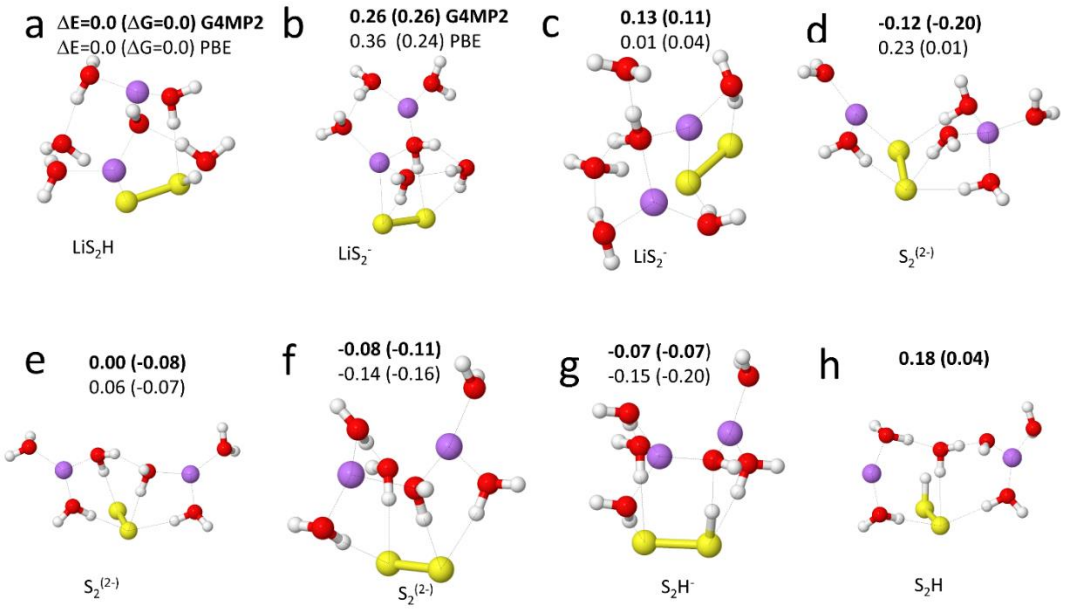

Figure S18. Relative energies (ΔE) and free energies (ΔG, in parentheses) for the Li_2S_2-$(H_2O)_6$ solvates from G4MP2 (in bold) and PBE/6-31+G(d,p) QC calculations in eV. PCM(water) polarized continuum model was utilized in all calculations.

The Li^+ dissociation and water decomposition in the longer Li_2S_4 polysulfide was examined using the Li_2S_4-$(H_2O)_8$ complexes as a model system as shown in Fig. S19. Again, PCM model was utilized to implicitly include solvent effects beyond the first eight water molecules that were explicitly included in QC calculations. We find that the contact ion pair (CIP, complexes a-c) LiS_4^- has a similar or even slightly higher energy than the fully dissociated complexes (d-f). All examined HS_4^- solvates (complexes g-j) have higher energy and lower stability than the SSIP $S_4^{(2-)}$ or LiS_4^- solvates indicating that water deprotonation near longer polysulfide s such as Li_2S_4 is unlikely. Water decomposition is, however, energetically favorable on the surface of $(Li_2S)_3$ clusters as shown in Fig. S20. Single protonation of the (Li_2S) clusters stabilizes them by as much as 0.39 eV when free water is available. Due to improved stability such clusters will form earlier during cell charging resulting in a flatter charging profile compared to standard aprotic electrolytes as shown in Fig. 2(C-D) in the main part of the manuscript.

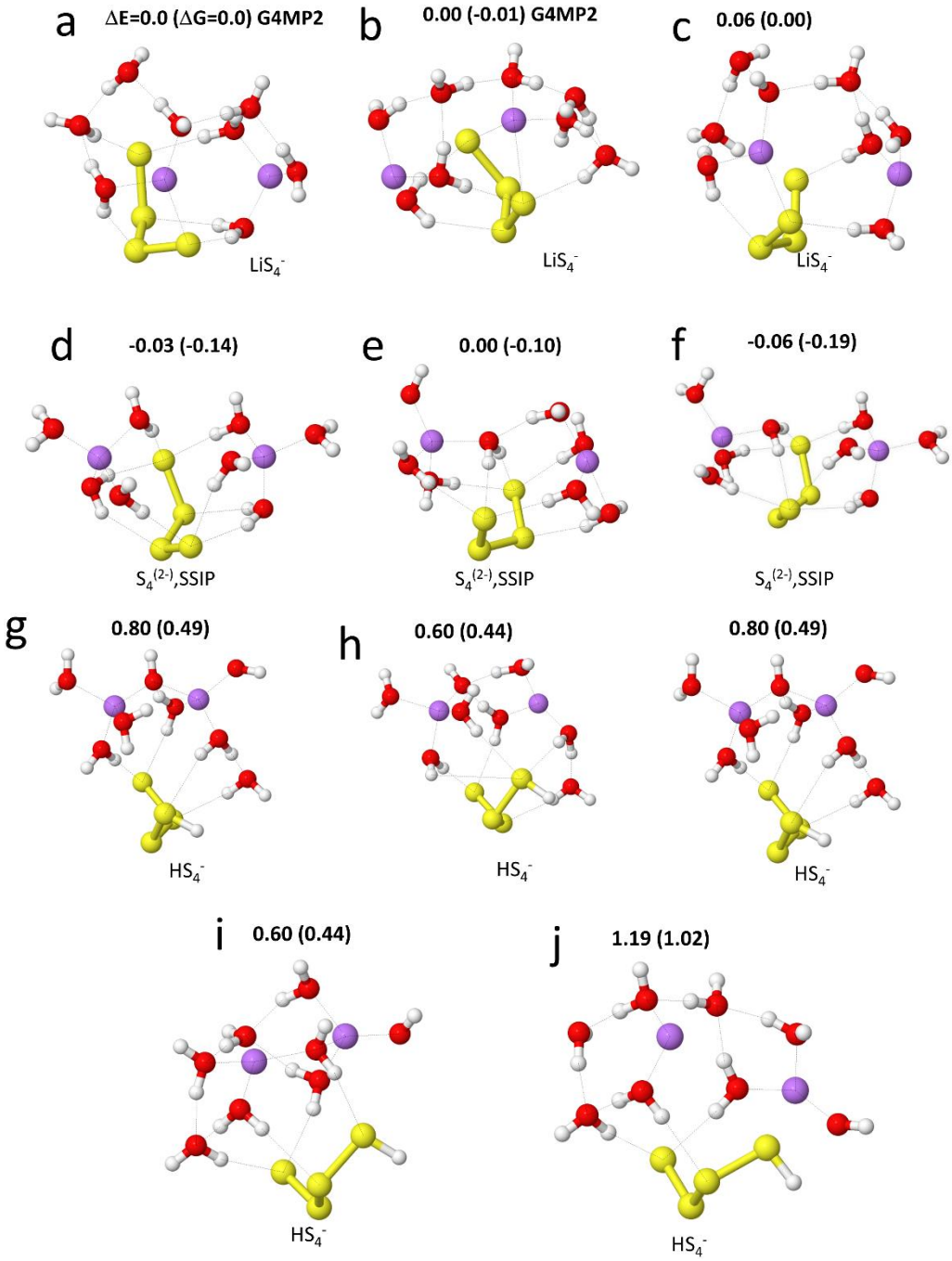

Figure S19. Relative energies (ΔE) and free energies (ΔG, in parentheses) for the Li_2S_4-$(H_2O)_8$ solvates from G4MP2 QC calculations in eV. PCM (water) polarized continuum model was utilized in all calculations.

In summary, we conclude that strong lithium dissociating propensity of water facilitates the Li_2S_2 and Li_2S_4 dissolution, suggesting that limiting the amount of free water is necessary to suppress Li_2S_2 and Li_2S_4 association, encourage aggregation and potentially to suppress their

solubility in aqueous electrolytes and hence reduce water decomposition. Short chain polysulfide s (Li_2S, Li_2S_2) are stabilized by water decomposition followed by H-S bond formation, while OH- and HS_4^- formation is energetically unfavorable for the longer chain polysulfide such as Li_2S_4.

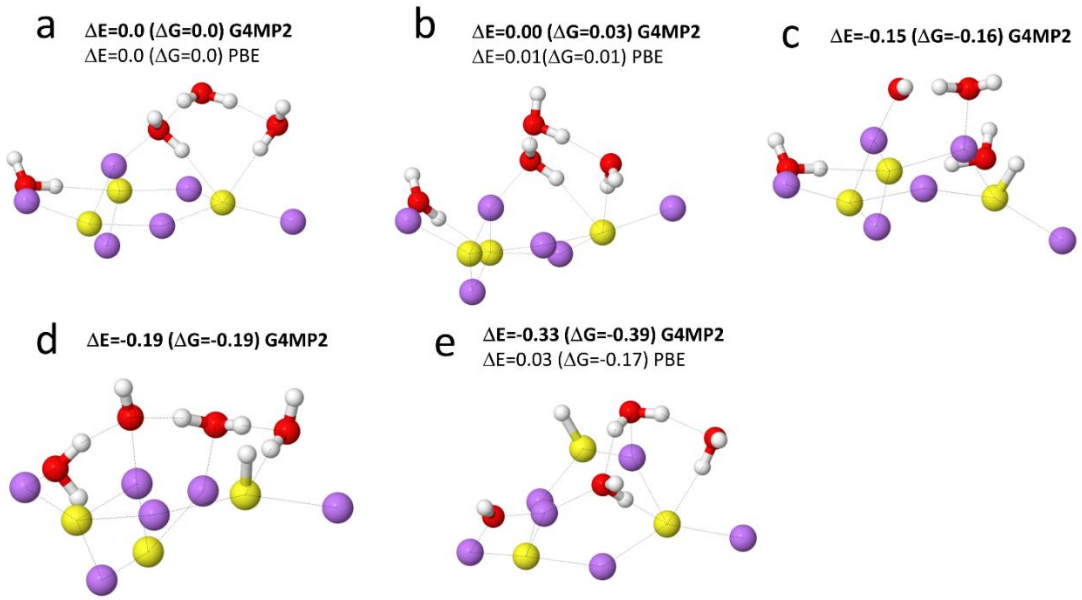

Figure S20. Relative energies (ΔE) and free energies (ΔG, in parentheses) for the $3Li_2S$-$(H_2O)_4$ solvates from G4MP2 (in bold) and PBE/6-31+G(d,p) QC calculations. PCM(water) polarized continuum model was utilized in all calculations.

In order to further examine the relative stability of the Li_2S_2 vs. Li_2S_4 solvates, free energy of the following reaction was calculated using the lowest energy solvates from Figures S18-S19 using eq. S1 that is equivalent to eq. S2:

$$Li_2S_4(H_2O)_8 + 2Li^+(H_2O)_4 \rightarrow 2(Li_2S_2(H_2O)_6) + (H_2O)_4 \quad \text{(S1)}$$

$$Li_2S_{4SOLV} + 2Li^+_{SOLV} \rightarrow 2(Li_2S_2)_{SOLV}, \quad \text{(S2)}$$

where the subscript SOLV denotes the solvated and dissociated species in electrolyte. This reaction was found exergonic with reaction free energy of -0.29 eV. Thus, the dissociated Li_2S_4 will convert to Li_2S_2 $+2Li^+$ (solvated) in aqueous electrolytes and the polysulfide equilibrium is shifted to shorter chain polysulfide molecules. Interestingly, previous DFT studies showed formation of Li_4S_8-like agglomerate in the LiTDI-salt based electrolyte that was more stable and compact than the

polysulfides formed in the LiTFSI-salt electrolyte indicating that a choice of anion could also influence polysulfide aggregation and disproportionation reactions (11).

Molecular Dynamics Simulations of Polysulfide s in Water and Bisalt Electrolyte

Force field for the Li_2S_2 and Li_2S_4 polysulfide salts was developed in this work following previously established methodology (12). It accurately described the Li^+ binging energy for the Li_2S_x (x=1, 2, 4) as shown in Fig. S17 and water binding energy to S_4^-. The $H_2O/S_4^{(2-)}$ binding energy was -19.5 kcal/mol from molecular mechanism using developed force field that is only slightly lower than the binding energy of -20.5 kcal/mol obtained from G4MP2 QC calculations. The previously developed and valided LiTFSI/water and $LiCF_3SO_3$/water force field parameters were used (13, 14). The Li^+ cation charge being set to 1e while the $TFSI^-$ and $CF_3SO_3^-$ anion charges were set to -1e. The Ewald summation method was used for the electrostatic interactions between permanent charges with permanent charges and permanent charges with induced dipole moments with $k = 7^3$ vectors. Multiple timestep integration was employed with an inner timestep of 0.5 fs (bonded interactions), a central time step of 1.5 fs for all nonbonded interactions within a truncation distance of 7.0-8.0 Å and an outer timestep of 3.0 fs for all nonbonded interactions between 7.0 Å and the nonbonded truncation distance of the smaller of 16 Å. The reciprocal part of Ewald was updated only at the largest of the multiple time steps. A Nose-Hoover thermostat and a barostat were used to control the temperature and pressure with the associated frequencies of 10^{-2} and 0.1 x 10^{-4} fs.

The in-house developed MD simulation package that includes many-body polarization, was used for all the MD simulations. Four electrolytes were simulated: (a) 4m Li_2S_2 in water; (b) 4m Li_2S_4 in water; (c) 4m Li_2S_2 in 21 mol kg^{-1} LiTFSI + 7 mol kg^{-1} $LiOCF_3SO_3$ denoted as 4m Li_2S_2 in water in bisalt salt electrolyte (WiBS); and (d) 4m Li_2S_4 in 21 mol kg^{-1} LiTFSI + 7 mol kg^{-1} $LiOCF_3SO_3$ denoted as 4m Li_2S_4 in WiBS. The MD simulation box comprised of 112 Li_2S_x (x=2,4) and 1536 waters for 4m salt in water electrolytes and 56 Li_2S_x (x=2,4), 96 $LiCF_3SO_3$, 288 LiTFSI and 768 waters for the polysulfide s in WiBS electrolytes. The initial configurations for simulations were created in the gas-phase with box sizes around 100 Å for the WiBS-based electrolyte and 75 Å for the sulfide s in water electrolytes. The simulation box dimensions were gradually decreased to 55 Å during 1 ns run at 500 K. Than the temperature was dropped to 450 K and NPT equilibration

runs were performed for 1.5 ns for 4 m Li_2S_4 in water electrolyte and 5 ns for Li_2S_4 in WiBS electrolyte using the force field with an additional repulsion between sulfides to facilitate their even distribution through the simulation box. The initial configurations of the Li_2S_2 in water and Li_2S_2 in WiBS electrolytes were generated from the final configurations of the corresponding systems with Li_2S_4 by removing two sulfur atoms from the S_4-chain. After that MD simulations were performed in order to examine the lithium polysulfide dissociation, aggregation and nano-separation. MD simulations of Li_2S_4 in WiBS were performed for 45 ns at 333 K. Since the experimental results also showed a sharp phase separation around 333 K (Fig. S8d), the higher temperature can accelerate MD simulations. Li_2S_4 in water was initially simulated for 4.0 ns at 363 K followed by 4.4 ns simulations at 333 K. MD simulations of Li_2S_2 in WiBS were performed for 8.0 ns at 393 K followed by 3.0 ns run at 333 K, while Li_2S_2 in water was simulated for 2 ns at 333 K. The initial and final configurations for the Li_2S_2 and Li_2S_4 in WiBS electrolytes and for Li_2S_2 and Li_2S_4 in water are shown in Fig. S21 and S22, respectively, highlighting the polysulfide anions and water.

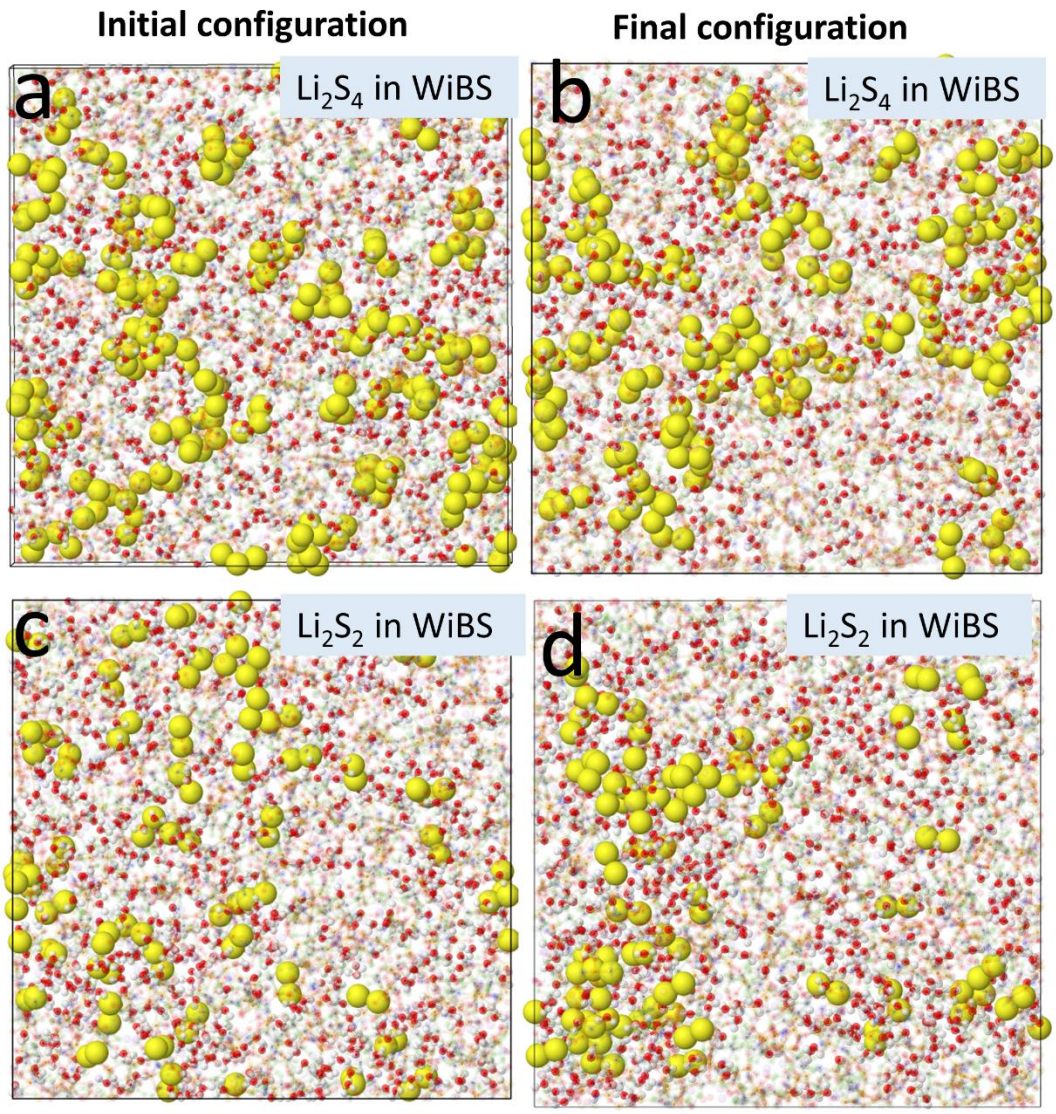

Figure S21. Projections of MD simulation boxes highlighting Li_2S_4 and Li_2S_2 polysulfide anions (color yellow) and water (color O:red, H:white) separating in WiBS electrolyte. Initial configurations (a,c) and final configurations (b,d) of MD simulations are shown.

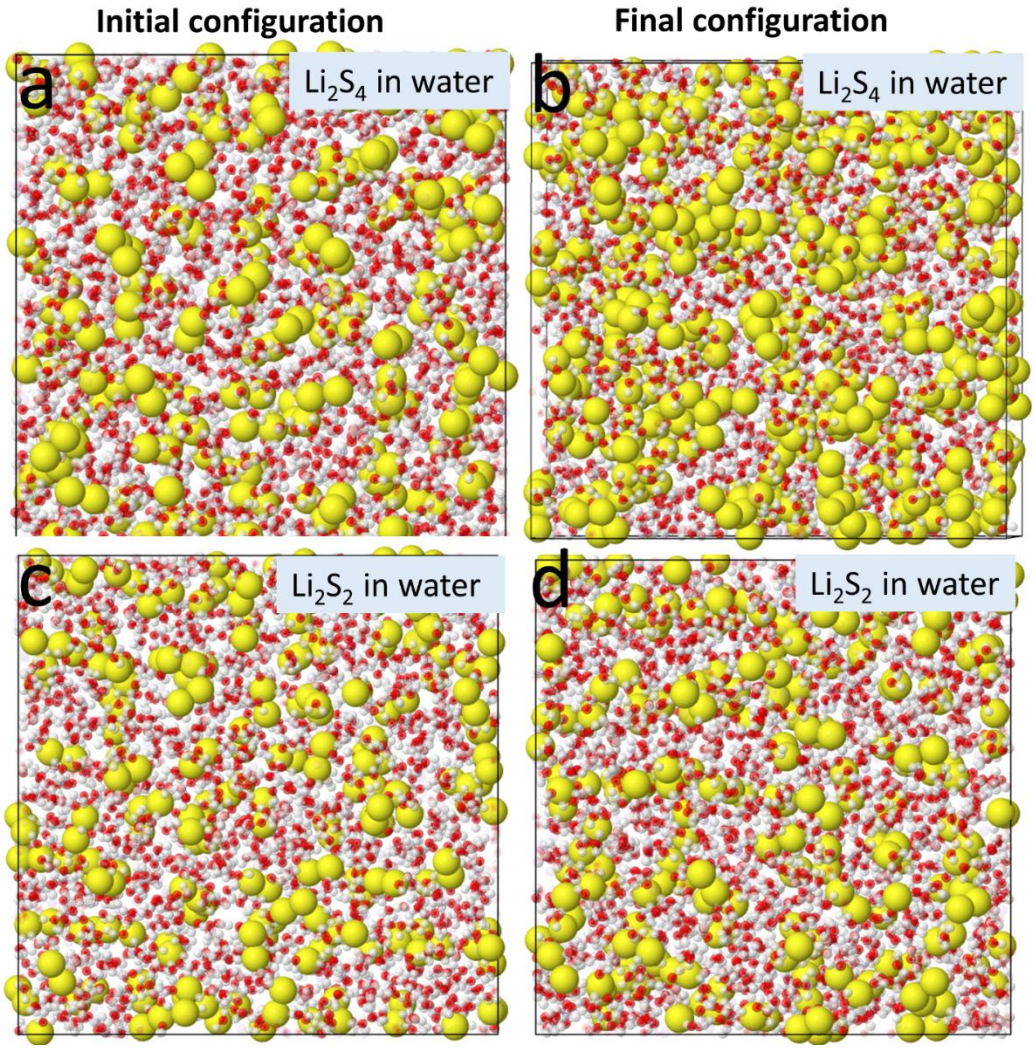

Figure S22. Projections of MD simulation boxes highlighting Li_2S_4 and Li_2S_2 polysulfide anions (color yellow) and water (color O:red, H:white) for Li_2S_4 in water (a-b) and Li_2S_2 in water (c-d). Initial configurations (a,c) and final configurations (b,d) of MD simulations are shown.

The Li_2S_4 polysufides were found to increasingly aggregate and separate in the WiBS electrolytes during MD simulations runs as shown in Fig. S21b. There is a domain without $S_4^{(2-)}$ in the MD simulations box that is formed during simulations. The shorter polysulfide anions $S_2^{(2-)}$ were found to exhibit even stronger aggregation and separation in the Li_2S_2 in WiBS electrolyte in the course of MD simulations than the observed $S_4^{(2-)}$ anion separation in the Li_2S_4 in WiBS electrolyte highlighting a stronger propensity of the shorter lithium polysulfide s to aggregate and separate into domains. Fig. S21 also shows that there is an enrichment of water near the polysulfide domain

compared to the rest of electrolyte indicating that water limitation is likely to limit the size of the solvated polysulfide domain. MD simulations of the Li_2S_2 and Li_2S_4 4m polysulfide solutions in water shows in Fig. S22 that both Li_2S_2 and Li_2S_4 are well dissolved and mixed. Most of the Li^+ cations were found to be solvent separated from polysulfide $S_4^{(2-)}$ and $S_2^{(2-)}$ anions in the Li_2S_2 in water and Li_2S_4 in water electrolytes in accord with QC results shown in Figures S18 and S19. We conclude that the results of MD simulations are in excellent agreement with the experimental observations showing phase separation of the lithium polysulfide s in WiBS electrolytes (see Fig. 2 of the main manuscript) and high polysulfide solubility in water.

Supplementary References

1. Cheng L, et al. (2016) Sparingly Solvating Electrolytes for High Energy Density Lithium–Sulfur Batteries. *ACS Energy Letters* 1(3):503-509.
2. Suo L, Hu Y-S, Li H, Armand M, Chen L (2013) A new class of Solvent-in-Salt electrolyte for high-energy rechargeable metallic lithium batteries. *Nat Commun* 4: 1481.
3. Lee JT, et al. (2013) Sulfur-Infiltrated Micro- and Mesoporous Silicon Carbide-Derived Carbon Cathode for High-Performance Lithium Sulfur Batteries. *Adv Mater* 25(33):4573-4579.
4. Ueno K, et al. (2013) Anionic Effects on Solvate Ionic Liquid Electrolytes in Rechargeable Lithium-Sulfur Batteries. *J Phys Chem C* 117(40):20509-20516.
5. Jonsson E, Armand M, Johansson P (2012) Novel pseudo-delocalized anions for lithium battery electrolytes. *Phys Chem Chem Phys* 14(17):6021-6025.
6. Scheers J, Jonsson E, Jacobsson P, Johansson P (2012) Novel Lithium Imides; Effects of -F, -CF_3, and -C equivalent to N Substituents on Lithium Battery Salt Stability and Dissociation (vol 80, pg 18, 2012). *Electrochemistry* 80(3):142-142.
7. Frisch MJT G W, et al. G09, Revision C. Wallingford CT, 2013: Gaussian, Inc.; 2013.
8. Bauschlicher CW, Haskins JB, Bucholz EW, Lawson JW, Borodin O (2014) Structure and Energetics of Li^+-$(BF_4^-)_n$, Li^+-$(FSI^-)_n$, and Li^+-$(TFSI^-)_n$: Ab Initio and Polarizable Force Field Approaches. *J Phys Chem B* 118(36):10785-10794.
9. Borodin O, et al. (2015) Electrolyte Solvation and Ionic Association: VI. Acetonitrile-Lithium Salt Mixtures: Highly Associated Salts Revisited. *J Electrochem Soc* 162(4):A501-A510.

10. Delp SA, et al. (2016) Importance of Reduction and Oxidation Stability of High Voltage Electrolytes and Additives. *Electrochimica Acta* 209:498-510.

11. Chen J, et al. (2016) Restricting the Solubility of Polysulfide s in Li-S Batteries Via Electrolyte Salt Selection. *Adv Ener Mater* 6(11):1600160.

12. Borodin O (2009) Polarizable Force Field Development and Molecular Dynamics Simulations of Ionic Liquids. *J Phys Chem B* 113(33):11463-11478.

13. Suo L, et al. (2015) "Water-in-salt" electrolyte enables high-voltage aqueous lithium-ion chemistries. *Science* 350(6263):938-943.

14. Suo L, et al. (2016) Advanced High-Voltage Aqueous Lithium-Ion Battery Enabled by "Water-in-Bisalt" Electrolyte. *Angew Chem Int Ed* 55(25):7136-7141.